SANDIA REPORT

SAND2007-6565
Unlimited Release
Printed January 2008

Desalination Utilizing Clathrate Hydrates (LDRD Final Report)

Robert W. Bradshaw, Jeffrey A. Greathouse, Randall T. Cygan, Blake A. Simmons, Daniel E. Dedrick, and Eric H. Majzoub

Prepared by
Sandia National Laboratories
Albuquerque, New Mexico 87185 and Livermore, California 94550

Sandia is a multiprogram laboratory operated by Sandia Corporation,
a Lockheed Martin Company, for the United States Department of Energy's
National Nuclear Security Administration under Contract DE-AC04-94-AL85000.

Issued by Sandia National Laboratories, operated for the United States Department of Energy by Sandia Corporation.

Available to DOE and DOE contractors from
U.S. Department of Energy
Office of Scientific and Technical Information
P.O. Box 62
Oak Ridge, TN 37831

Telephone: (865) 576-8401
Facsimile: (865) 576-5728
E-Mail: reports@adonis.osti.gov
Online ordering: http://www.doe.gov/bridge

Available to the public from
U.S. Department of Commerce
National Technical Information Service
5285 Port Royal Rd
Springfield, VA 22161

Telephone: (800) 553-6847
Facsimile: (703) 605-6900
E-Mail: orders@ntis.fedworld.gov
Online order: http://www.ntis.gov/help/ordermethods.asp?loc=7-4-0#online

SAND2007-6565
Unlimited Release
Printed January 2008

Desalination Utilizing Clathrate Hydrates (LDRD Final Report)

Robert W. Bradshaw
Materials Chemistry Department

Daniel E. Dedrick
Thermal/Fluid Science and Engineering Department

Blake A. Simmons
Energy Systems Department

Sandia National Laboratories
P. O. Box 969
Livermore California 94550

Jeffrey A. Greathouse and Randall T. Cygan
Geochemistry Department
Sandia National Laboratories
P. O. Box 5400
Albuquerque, New Mexico 87185

Eric H. Majzoub
University of Missouri
210 Jesse Hall
Columbia, MO 65211

Abstract

Advances are reported in several aspects of clathrate hydrate desalination fundamentals necessary to develop an economical means to produce municipal quantities of potable water from seawater or brackish feedstock. These aspects include the following, (1) advances in defining the most promising systems design based on new types of hydrate guest molecules, (2) selection of optimal multi-phase reactors and separation arrangements, and, (3) applicability of an inert heat exchange fluid to moderate hydrate growth, control the morphology of the solid hydrate material formed, and facilitate separation of hydrate solids from concentrated brine. The rate of R141b hydrate formation was determined and found to depend only on the degree of supercooling. The rate of R141b hydrate formation in the presence of a heat exchange fluid depended on the degree of supercooling according to the same rate equation as pure R141b with

secondary dependence on salinity. Experiments demonstrated that a perfluorocarbon heat exchange fluid assisted separation of R141b hydrates from brine. Preliminary experiments using the guest species, difluoromethane, showed that hydrate formation rates were substantial at temperatures up to at least 12°C and demonstrated partial separation of water from brine.

We present a detailed molecular picture of the structure and dynamics of R141b guest molecules within water cages, obtained from ab initio calculations, molecular dynamics simulations, and Raman spectroscopy. Density functional theory calculations were used to provide an energetic and molecular orbital description of R141b stability in both large and small cages in a structure II hydrate. Additionally, the hydrate of an isomer, 1,2-dichloro-1-fluoroethane, does not form at ambient conditions because of extensive overlap of electron density between guest and host. Classical molecular dynamics simulations and laboratory trials support the results for the isomer hydrate. Molecular dynamics simulations show that R141b hydrate is stable at temperatures up to 265K, while the isomer hydrate is only stable up to 150K. Despite hydrogen bonding between guest and host, R141b molecules rotated freely within the water cage. The Raman spectrum of R141b in both the pure and hydrate phases was also compared with vibrational analysis from both computational methods. In particular, the frequency of the C-Cl stretch mode (585 cm^{-1}) undergoes a shift to higher frequency in the hydrate phase. Raman spectra also indicate that this peak undergoes splitting and intensity variation as the temperature is decreased from 4°C to -4°C.

Acknowledgments

The authors gratefully acknowledge the contributions to this study made by Bill Anderson (8758) for laboratory support modifying and operating the experimental hydrate cell and Miles Clift (8758), who performed cold-stage x-ray diffraction of R141b hydrate samples.

We acknowledge support for this work by the LDRD Program at Sandia National Laboratories. Sandia National Laboratories is a multiprogram laboratory operated by Sandia Corporation, a Lockheed Martin Company, for the United States Department of Energy's National Nuclear Security Administration under Contract DE-AC04-94AL85000.

This page has been intentionally left blank

Contents

This page has been intentionally left blank

List of Figures

List of Tables

This page has been intentionally left blank

1. Introduction

Potable water is presently produced from seawater or brackish water by either reverse osmosis (RO) or multi-stage flash distillation (MSF), the latter depending on the availability of inexpensive fossil fuels to generate the thermal energy required. These processes are in large-scale use in regions that have serious shortages of fresh water such as the Arabian Peninsula. One of the few examples of desalination for municipal water supplies in the U.S. is the Mid-Pinellas RO project in the Tampa, FL region, which will provide 5 million gallons per day from brackish water when complete.[1] A larger RO facility to process seawater is planned by the City of Huntington Beach in southern California.[2] Many other areas of the U.S.A. are considering desalination facilities to satisfy their future potable water needs. Thus, the cheap and efficient production of plentiful fresh water is becoming increasingly important to the sustainability our national infrastructure. This report describes advances in our understanding of clathrate hydrates as an alternative method for the effective desalination of seawater or brackish water to meet this goal.

Clathrate hydrates are crystalline inclusion compounds of water (majority specie) and a guest molecule (minority specie) that form spontaneously at conditions of temperature and pressure particular to each guest molecule. The temperatures at which these clathrate hydrates are stable are typically somewhat above the freezing point of water, although some guest molecules stabilize hydrates at nearly ambient temperature. There are three recognized crystalline structures that clathrate hydrates can possess, structure I, structure II and structure H. Each of these crystalline types contains cage-like sub-structures that are formed by the water molecules and enclathrate the guest molecule within. The organization of water molecules in the sub-structures of these three clathrate hydrates are shown in Figure 1. These structures obviously differ markedly from the common hexagonal structure of solid water (ice). Structure I (sI) hydrates have unit cells comprised of 46 water molecules with six cages that can contain small gas molecules, such as methane and ethane. The unit cell of structure II (sII) hydrates is comprised of 136 water molecules with 24 cages that can hold somewhat larger gas molecules, such as propane and isobutene.

Although hydrogen bonding is the primary water-water interaction in hydrates, the guest molecules are stabilized within the cages by Van der Waals forces. After a sufficient number of the cages are occupied, (~70-75%) a thermodynamically stable, crystalline unit cell structure is formed. These hydrates are commonly referred to as gas hydrates and often contain guest molecules that predominantly exist in the gas phase at standard temperature and pressure. The most abundant naturally occurring gaseous hydrate is formed by methane, but numerous other gases, including carbon dioxide, hydrogen sulfide, ethane, ethylene, and propane, also form hydrates. Many other guest molecules have been identified that are sufficiently small to fit within the cage sub-structures and thereby stabilize hydrates.[3]

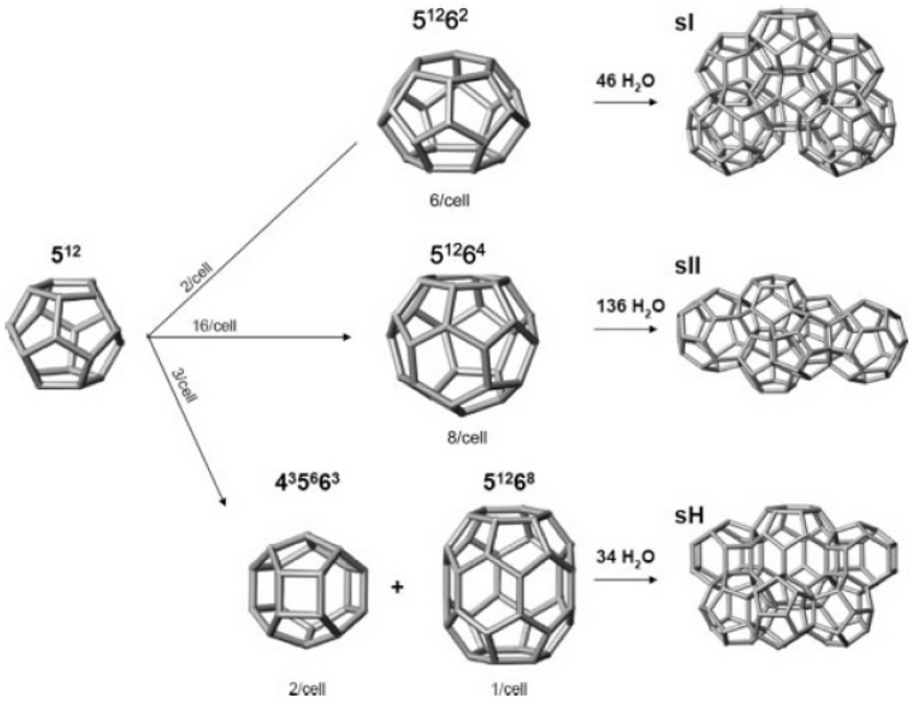

Figure 1. Structures of sI, sII and sH clathrate hydrates. The vertices of the cage sub-structures are the locations of water molecules which enclathrate a single guest molecule. (Koh and Sloan, 2007 [4])

1.1 Previous Development of Clathrate Hydrate Desalination

The use of clathrate hydrate-forming agents to facilitate freeze desalination of saline water has been investigated by a number of groups with significant efforts starting in the 1960's. Koppers Co. developed a hydrate desalination process based on propane.[5, 6] Barduhn and associates investigated a variety of hydrate forming compounds and studied kinetics and separations in continuous flow systems.[7] The Bureau of Reclamation has recently commissioned work from Thermal Energy Systems, Inc., to explore the feasibility of this technology and the creation of two pilot plant facilities, one in Hawaii and a subsequent effort in San Diego.[8-10] The process developed by Thermal Energy Systems directly injected a hydrochlorofluorocarbon (HCFC) refrigerant, R141b, into a pressurized tank of seawater at hydrate-forming conditions (typically 100 psig and 5°C). This produced a complex slurry of hydrates and brine from which the hydrates must be recovered and purified before disassociation. The hydrates formed were small and dendritic with a high amount of salt entrapped in the interstitial spaces. To solve this problem they utilized filtration to remove the smallest hydrates and a wash column to remove the excess salt from the remainder. This wash step produced hydrates with potable water quality as per TDS requirements, but it was also this step that proved to be the largest detriment to overall process efficiency.[11] Even with the mixed results from this work, it was estimated that the cost associated with this technology would produce water at \$0.46 – \$0.52/m^3 with public funding.[8] This estimate, although based on a process yet to run on a completely functional level, is

comparable to the cost associated with other current desalination technologies such as reverse osmosis ($0.45-$0.92/ m^3) and multi-stage flash distillation ($1.10 - $1.50/ m^3).[12]

Clathrate hydrate desalination is not on the horizon as it stands now, as there are no operational facilities running on a continuous basis, even at the pilot plant scale. Before hydrate desalination is realized as a viable commercial technology, the fundamental issues of controlled hydrate nucleation, hydrate size and morphology, agglomeration, amount of entrapped salt, and the efficient recovery of hydrates must be thoroughly and effectively solved and optimizations implemented. Key to this goal is the elimination of a wash column, which would greatly enhance overall system efficiency by decreasing the amount of systems engineering. We propose to utilize a fundamental scientific approach to address these problems from the "bottom-up", i.e. studying and controlling hydrate nucleation and nucleation environment to bypass the necessity of a wash column. This approach is in contrast to the "top-down" approaches employed by the hydrate community thus far. This approach will result in the development and implementation of a fundamental enabling technology to be deployed within the existing systems engineered architecture for hydrate desalination.

1.2 Scope of LDRD Study

We attempted to solve the problem of interstitial salts and the necessity of using wash columns through parallel research efforts. We employed the extensive fundamental materials science and computational modeling at Sandia in both of these efforts. In the first area of research, we investigated novel hydrate formers that would allow for hydrate formation significantly above the freezing point of water and thus different nucleation environments. We began this work by using R141b, a substance that has been studied previously for desalination, and extended our work to hydrofluorocarbons, such as HFC-32, which have been identified as promising candidates in the literature.[8] We conducted experiments to determine the impact that these hydrate formers have on the nucleation environment and the extent to which this environment can be tailored to produce hydrates with the desired morphological characteristics (i.e. no dendritic growth and entrapped salt). We also investigated the possible utilization of additives to inhibit dendritic hydrate growth and thus minimize interstitial salt entrapment. We conducted fundamental studies into the rate of nucleation and crystallization of these hydrates at a variety of experimental conditions (e.g. pressure, temperature, flow rate) to develop an extensive knowledge base from which to operate.

Directly coupled with this effort was the first-principles computational modeling of these systems and their corresponding nucleation kinetics. Molecular modeling of the stability of the various clathrate hydrates will be performed in support of the experimental work. Specifically, we evaluated the relative stabilities of candidate gas clathrates (typically Structure I and Structure II compounds) using energy optimization and molecular dynamics methods. The latter method allows us to determine the P-T phase limits for each of the clathrates and helps constrain the experimental conditions of the water treatment process, especially for clathrates for which limited literature data are available. We validated the modeling with comparisons to measured data. These methods will be most helpful in monitoring the complex behavior of mixed gas clathrates where water-gas A, water-gas B, gas A-gas A, gas B-gas B, gas A-gas B, and water-

water interactions can be clearly defined and sorted in order to improve the efficiency of the desalination process.

In the second area of research, we investigated the formation of hydrates by directly contacting saline water with hydrate forming species that were dissolved in an inert heat exchange fluid. This approach is potentially novel and commercially valuable. The ideal heat exchange fluid would have the following properties: immiscibility with water, not form hydrates, and dissolve a significant amount of the hydrate forming species. Candidates for the heat exchange fluid included fluorocarbons, short and long-chain non-polar alkanes and associated fatty acids. The heat exchange fluid is placed in a pressure vessel and cooled to the appropriate hydrate forming temperature by immersing it in a temperature controlled water bath. The heat exchange fluid is then pressurized to the corresponding hydrate forming conditions with the hydrate forming species. For those salts that precipitate from solution, we will select the desired hydrate buoyancy type to separate the hydrates from the contaminants. This will prevent mixing of the two species and decrease the post-processing required to recover the pure water that has been converted to hydrates. A direct comparison of typical hydrate density (~0.91 g/cm^3) and the density of the most common salt, NaCl (2.17 g/cm^3) indicates that this phenomenon will be highly efficient in the separation of hydrates from the salts present. This process may also allow for the easy disposal of the brine salts in a solid form, which would greatly enhance the overall efficiency and desirability of the system.

2. Experimental Methods

Clathrate hydrate experiments were performed to observe the rates of hydrate formation and the physical characteristics of hydrate material using a variety of guest molecules and to determine the effect of heat exchange fluids on hydrate formation and separation properties. Experiments were performed using a variety of guest molecules in either the liquid or gaseous state. The guest species included a liquid guest, R141b (a refrigerant), and gaseous hydrate formers, difluoromethane, difluoroethane, and ethylene.

2.1 Apparatus

The hydrate cell enabled investigation of nucleation and growth of clathrate hydrates from gaseous and liquid hydrate formers under controlled environmental conditions. The basic design chosen for the experimental apparatus was a stirred batch reactor in which an aqueous phase could be mixed with a guest molecule, either in the liquid or gas state, and with a heat exchange fluid, if used for a particular experiment. The batch reactor was chosen because it is a simple system to operate and requires relatively little material for each experiment compared to the much larger throughput needed to operate a continuous flow stirred reactor. Minimizing the amounts of materials consumed enabled a broad range of hydrate guest molecules to be investigated during extensive parametric studies of the dependence of hydrate formation rates upon temperature, salinity, and pressure as well as the effect of heat exchange fluids and mixture proportions with hydrate forming agents. Batch reactors necessarily operate under transient or unsteady-state conditions during growth of hydrates, which may somewhat complicate analysis of kinetic data compared to the continuous reactor, which can operate at constant, steady-state conditions.

A Parr Model 4562 stirred pressure cell (Parr Instrument Co., Moline, IL) was assembled to conduct clathrate hydrate experiments using various guest molecules. The experimental cell was capable of working pressures up to 1500 psi and the volume of the reactor was approximately 500 ml. The experimental cell included a magnetically coupled stirrer shaft and stirring motor speed controller. The cell was jacketed to allow for temperature control by circulating a coolant from a Haake Model F3 thermostatic circulating bath. A schematic of the experimental system is shown in Figure 2 and includes a feed system for guest gas, an injection pump for water, temperature and pressure measurement devices and a data acquisition PC. Guest species could be supplied to the cell as either liquid or gas from an external reservoir if not loaded initially. Similarly, the aqueous phase could be pumped into the cell if not present initially. The large majority of hydrate formation experiments were done in simple batch mode. Photographs of the apparatus are shown in Figures 3 and 4.

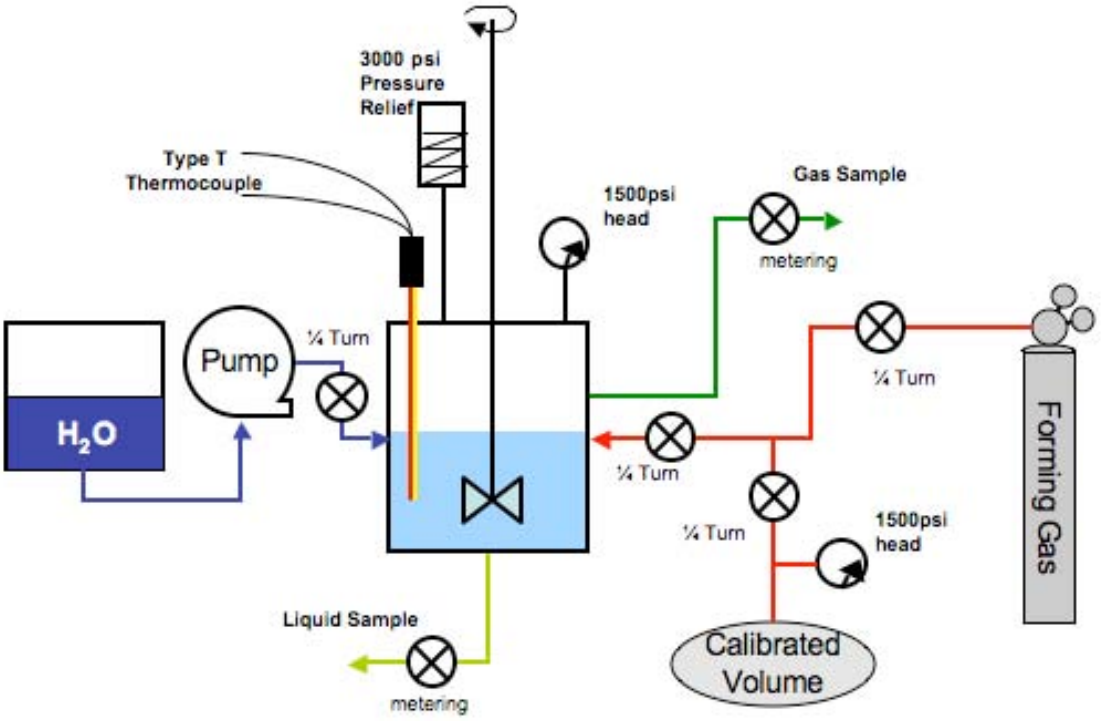

Figure 2. Schematic of the stirred, thermostatically controlled pressure cell used for hydrate formation experiments.

The temperature instrumentation for the hydrate cell consisted of a Type T and a Type K thermocouple inserted through compression fittings in the cell head into the liquid phases where hydrate growth occurred. The inserted thermocouples were compared to NIST-traceable thermocouples and the indications of the former were corrected for the difference by the data acquisition system software. The cell pressure was measured using Honeywell model PPTR1500AP2VB pressure transducers when gaseous guest molecules were used. One pressure transducer was attached to the head assembly of the Parr cell and the other to the cell gas inlet manifold, as shown in Figure 4. The pressure transducers that were periodically calibrated against a NIST-traceable pressure transducer. Temperature and pressure data were collected using an Agilent Model 34970A recording system, which was controlled by the Agilent data acquisition software application BenchLink. A complete set of data channels were acquired every 6 seconds, which was more than adequate time resolution for the hydrate formation experiments.

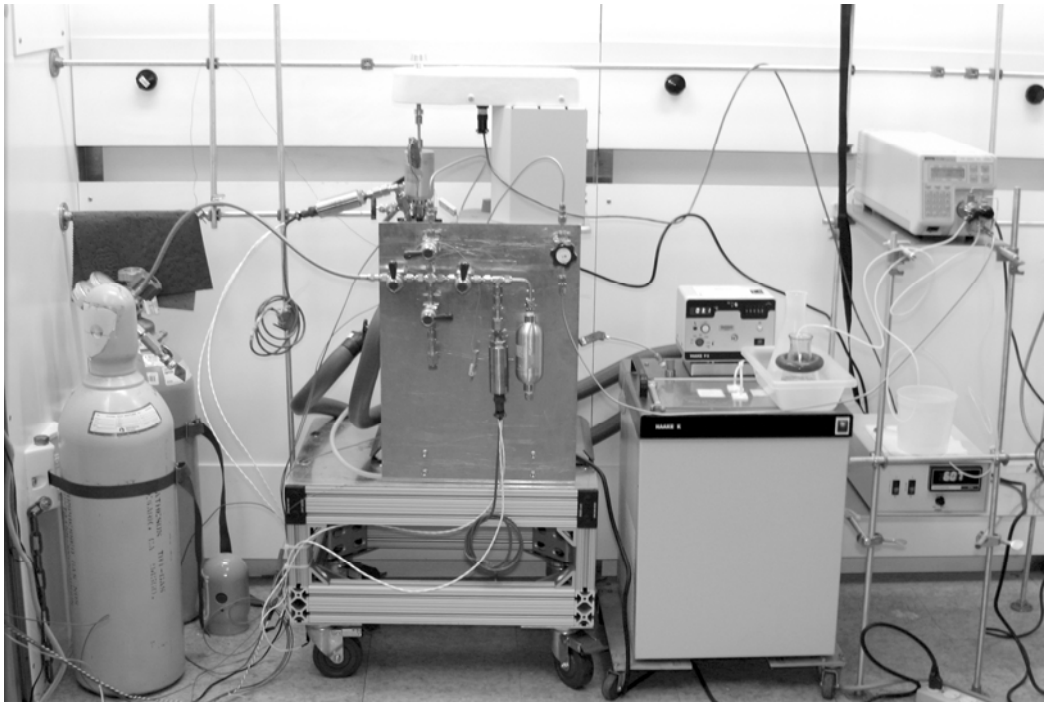

Figure 3. **View of complete Hydrate Cell apparatus showing thermostatic circulator, stirrer motor controller, injection pump.**

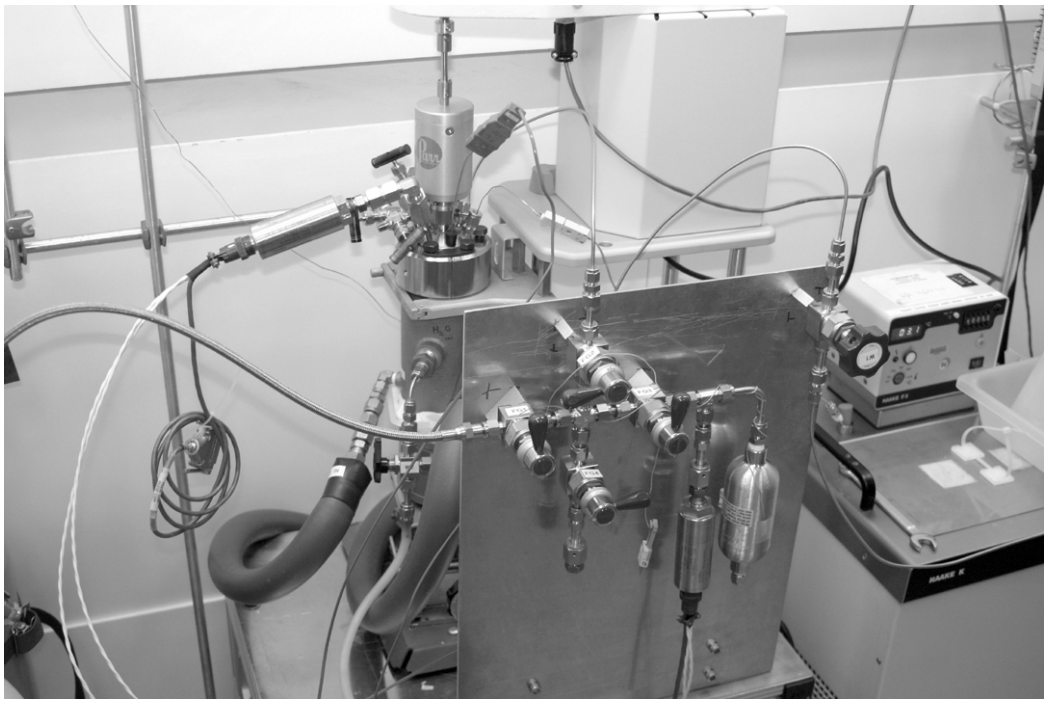

Figure 4. **Detail view of Hydrate Cell apparatus showing pressure cell and stirrer head, gas distribution manifold, pressure transducers and temperature instrumentation.**

2.2 Materials

The guest molecules used for hydrate formation experiments were R141b (1-fluoro, 1,1-dichloroethane, CAS 1717-00-6), ethylene (CAS 74-85-1), HFC-32 (difluoromethane, CAS 75-10-5), and R152a (difluoroethane, CAS 75-37-6). Ethylene, 99.5% pure, was obtained from Matheson Tri-Gas, Fremont, CA. HFC-32, 99.5%, and R152a, 99%, were obtained from Synquest Laboratories, Inc., Alachua, FL. Cyclopentane (CAS 287-93-2) was used as cooperative guest molecules when HFC-32 or R152a were the primary guest molecules. Saline solutions were prepared from deionized water (18 meg-ohm specific resistivity, produced by a NanoPure ion exchange system) and NaCl, ACS reagent grade, used as received. Fluorinert FC3283 was used as an inert heat exchange fluid (discussed later in the report) in many experiments. Fluorinert FC3283 (3M Co., Inc.) is a mixture of perfluorocarbons having an average molecular weight of 571, a boiling point of 128°C, density of 1.82 gm/cm^3 and a heat capacity of 0.25 cal/gm/°C, according to the manufacturer's datasheet.

2.3 Procedure

R141b hydrate experiments were performed by adding weighed amounts of chilled R141b to the cell in which a weighed amount of saline solution had been added and chilled to the test temperature. The two liquid phases were stirred at a low rotation speed until the immersed thermocouples indicated stable temperatures at the desired value. Seed crystals were added and the cell head secured without flushing the cell after it was closed, as the presence of air did not affect the observed hydrate formation. The stirrer speed was increased to 600 rpm and hydrate growth ordinarily commenced shortly thereafter. The formation of hydrates was ordinarily indicated by an abrupt increase in the temperature of the cell contents, as measured by two inserted thermocouples.

Approximately 0.1 gram of R141b hydrate seed crystals were added to the chilled contents of the cell from hydrate material grown separately and stored in a refrigerator. Secondary nucleation by the added seed material caused sustained growth of R141b hydrates with little apparent induction time. Primary, or homogeneous, nucleation gives rise to long, variable induction times before onset of hydrate growth.[13] Primary nucleation also has the disadvantage that it represents an environment that is intrinsically different from a production-scale hydrate reactor, which would always have a significant amount of solid hydrate material present.

Hydrate experiments with gaseous guest molecules were performed by adding a weighed amount of saline solution to the cell and chilling to the test temperature while stirring at a low rotation speed to attain steady-state values. The cell head was secured and the internal gas volume flushed with argon several times before admitting gaseous hydrate guest molecules. The pressure was maintained at above 100 psi during the final argon purge with the cell sealed to assure that the pressure maintained a constant value, which indicated that no leakage would occur during the test period. The guest gas was admitted into the cell at the desired pressure, the valves closed, and the stirrer rotated at 600 rpm. Homogeneous nucleation was ordinarily used with gas guest species as seed material was neither practical, because of the need to maintain high pressure to

stabilize the seed crystals, nor necessary for this type of hydrate formation environment. The formation of hydrates was ordinarily indicated by a sustained increase in the temperature of the cell contents, as measured by two inserted thermocouples, and was also indicated by a continuous decrease in the cell pressure as the guest was incorporated into solid hydrates.

Samples of hydrate material were recovered at atmospheric pressure after the cell head was removed to provide access to the cell. Hydrate samples were recovered by scooping material from the cell with a chilled spatula, placing it in a pre-chilled vial and storing in a freezer if analysis was to be performed subsequently. Otherwise, hydrate samples were allowed to melt and the salt content determined by measuring the refractive index. Salt separation was also determined by measuring the refractive index of the initial and final saline phase. Refractive index measurements were performed using an Leica Abbe refractometer (Reichert Co., Depew, NY, Model 1310499SA). The refractive index data were converted to the corresponding concentration of NaCl in the solution using a published correlation.[14]

2.4 Mixing

Mixing is an important parameter in the experimental measurements because most hydrate formation experiments were necessarily conducted in multi-phase systems consisting of one or two liquid phases, the solid hydrate phase, which increased in mass with time, and a gas phase. The impeller type was a 4-blade Parr propeller in most experiments and was rotated at the same speed of 600 rpm in virtually all experiments. The impeller was located within the more dense liquid layer, i.e., R141b or an R141b-Fluorinert mixture. This location produces agitation such that the less dense liquid is dispersed in the more dense liquid.[15,16] The impeller was partially immersed at the liquid layer when gaseous guest molecules were used in order to create an appreciable surface area for gas-liquid contact.

To better understand the possible implications of liquid-liquid mixing on hydrate formation rates, we made observations of mixing using a clear Lexan visualization cell the same size as the Parr hydrate cell. This visualization cell was filled with the same amounts of liquids used in various types of hydrate formation experiments. The pressure cell head with the magnetic drive and impeller was inserted into the clear plastic cell in the same manner as the hydrate formation cell and rotated at a variety of speeds spanning the range used for hydrate experiments to observe variations in the fluid flow and dispersion patterns. The observations of the dispersion of saline and an immiscible organic liquid were very useful with regard to ascertaining the effect of stirrer rotation speed and the behavior of various impellers shapes and locations. However, these observations were limited by the absence of the solid material present when hydrates were formed. We used a borescope camera to visualize agitation within the Parr pressure cell during hydrate formation in a few experiments and recorded by still photographs and videos. These observations confirmed the behavior seen in the Lexan cell.

The experimental details of structural analysis of hydrate materials by Raman spectroscopy and X-ray diffraction are discussed in a later section of the report.

This page has been intentionally left blank

3. R141b Hydrate Formation Kinetics

The use of an inert fluid to facilitate controlled formation and separation of clathrate hydrates formed by another agent and water was suggested by the work of Irvin, et al, [17], who employed the clathrate hydrate phenomenon to prepare nanoparticles of inorganic materials. The applicability of such an inert "heat exchange fluid" to clathrate hydrate desalination, in which hydrates must be formed and subsequently separated from the residual brine, was investigated using combinations of guest molecules and heat exchange fluids as discussed later in this report. This technique appears to be novel and a patent application has been filed.[18] R141b is an excellent starting point to determine the applicability of the heat exchange fluid method in general as it has been used previously as the basis for development of a desalination process.[8-10] Many studies of R41b hydrate formation have been published that have considered applications for cool storage, [19, 20] as well as fundamental studies of nucleation and hydrate formation.[21-23] However, no published reports provide any information regarding the rate at which hydrates form between the liquid guest molecule and the aqueous phase in an experimental configuration that is relevant to desalination applications.

Rate of formation data are important to determine the size of a hydrate desalination system for a given production capacity. The rate of hydrate formation is a critical factor in scaling up an experimental system to the size required for a realistic desalination process. Although the characteristics of mixing are very important for large-scale systems, rate data at the laboratory scale can indicate if a large-scale process is realistic and establish a basis for optimization during scale-up.

Hydrate formation experiments were conducted using R141b to provide a baseline for the effect of a heat exchange fluid on clathrate hydrate formation. R141b forms a sII hydrate in which the guest occupies most of the large cages of the unit cell. The thermodynamic stability of R141b hydrates have been studied by several groups.[24-26] The phase diagram (Figure 5) shows that the critical stability temperature is 8.4°C and the critical stability pressure is 40.2 kPa. The boiling point of R141b is 38°C, so R141b was in the liquid state in the experiments described below and thus hydrate formation occurred during liquid-liquid contact of guest and host molecules.

A matrix of R141b hydrate formation experiments were conducted at temperatures between 1°C and 7°C and saline concentrations of 0-7 wt.% NaCl to assess the rate of hydrate formation and the type of macroscopic hydrate aggregation. In some of these experiments, separation behavior of hydrates from brine was determined. We performed a total of 36 experiments, including several replicates. Rate data were extracted from measurements relating the temperatures of the hydrate-liquid-liquid slurry in the reactor to time of growth of hydrate material. Figure 6 shows the temperature-time profile of a typical R41b hydrate experiment. The temperature was measured at two locations in the slurry and both thermocouples ordinarily displayed the same rate of temperature increase as shown in the graph. At the outset of hydrate growth, the temperature gradually increases as hydrate formation is stimulated by secondary nucleation due

to the addition of seed material (see Experimental Section). Following this acceleration period, a linear temperature ramp was observed that typically persists for a significant portion of the hydrate growth phase in the cell. The temperature increase then decelerates and reaches a plateau that is limited by the equilibrium temperature for hydrate formation.

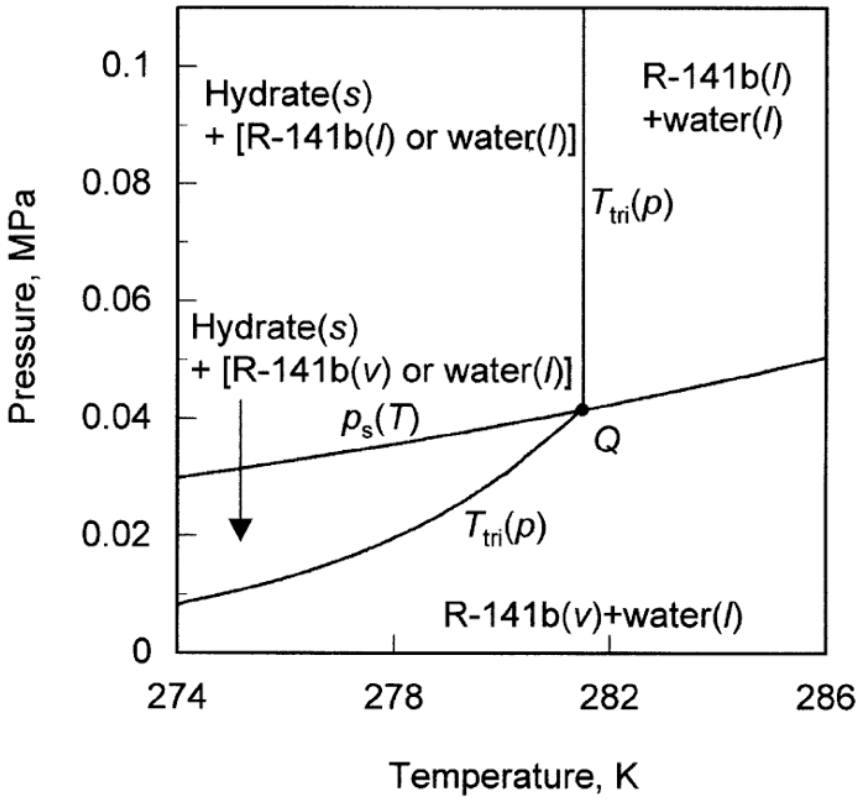

Figure 5. Phase diagram of the R141b clathrate hydrate system according to Ohmura, et al, 1999.[23] The point, Q, represents the highest temperature at which R141b hydrates are stable in contact with water.

The linear portion of the temperature-time profile is common to every rate experiment in which R141b hydrates were formed. Although the fundamental significance of this characteristic is not clear, the linear growth phase establishes a reasonable basis for comparing rate data from the matrix of experiments conducted at various dissolved salt concentrations and initial temperatures. The straight line in Figure 6 indicates the linear section of the temperature-time profiles used to calculate the apparent rate of hydrate formation according to the analysis described below.

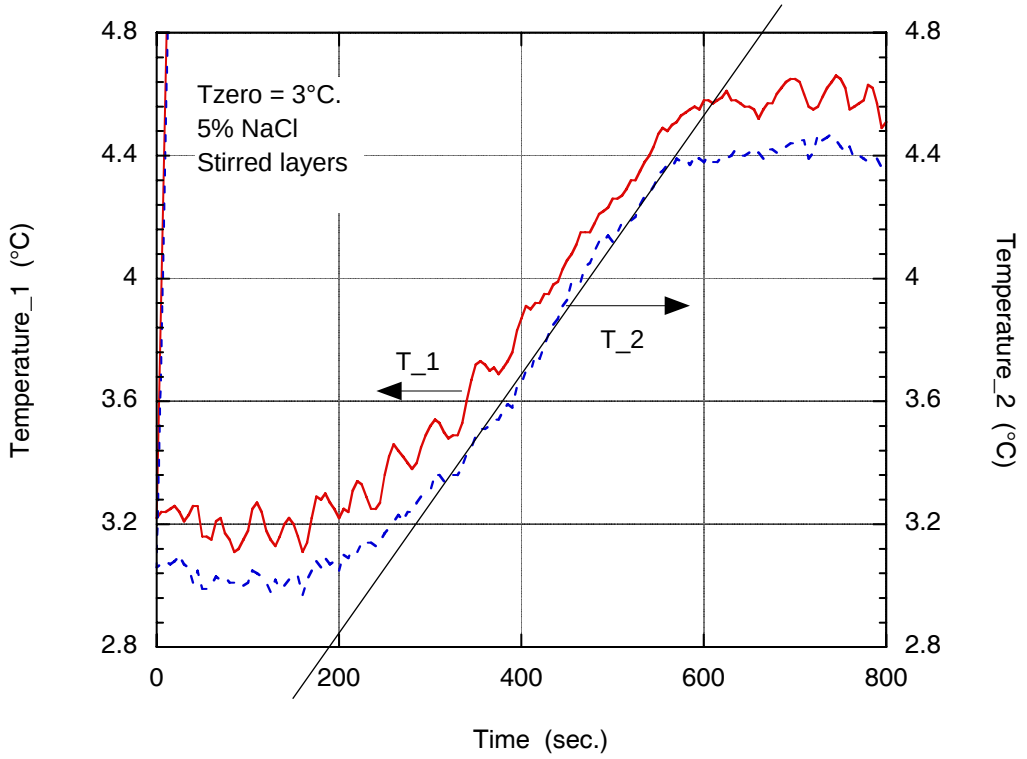

Figure 6. **Temperature-time profiles in a stirred batch reactor during R141b clathrate hydrate formation in 5% saline solution at an initial temperature of 3°C. The temperature at two locations in the R141b-hydrate-saline slurry is given by the left and right ordinates. The offset is due to the characteristics of the individual thermocouples. The straight line superimposed on the curves indicates the linear section of the temperature-time profiles that was used to calculate the apparent rate of hydrate formation. Both thermocouples displayed the same rate of temperature increase.**

The experimental system is initially comprised entirely of water (or saline solution) and liquid R141b. Hydrate formation is an exothermic process, so the enthalpy of fusion as hydrates are formed is manifested in the system as sensible heat that increases the temperature of the material in the cell. To relate the rate of this energetic process to the rate of formation of hydrates, we assume that the system is adiabatic and neglect the relatively small mass of the immersed stainless steel components. The rate of hydrate formation multiplied by the enthalpy change of hydrate formation equals the rate of temperature increase multiplied by the summed mass and heat capacity of the cell contents. The relationship between hydrate growth and the temperature of the growth media is given by the equation below.

$$R,hyd * H,w = \{ T/ t\} * \{M,w*Cp,w + M,g*Cp,g \} \qquad \text{Equation (1)}$$

where the quantities are defined as
R,hyd [=] hydrate formation rate; mols water/sec
{ T/ t} [=] rate of temperature increase during hydrate growth; °C/sec

Hw [=] enthalpy change of hydrate formation per mol water; cal/mol
M,w [=] mass of water or saline initially in cell
M,g [=] mass of guest specie (R141b) initially in cell
Cp,w [=] specific heat capacity of water or saline
Cp,g [=] specific heat capacity of guest specie (R141b)

The rate of hydrate formation is expressed above as the rate of incorporation of water molecules into the hydrate rather than the rate of formation of the hydrate itself. The former rate translates directly to water production rates for desalination system design. The enthalpy of formation of the sII clathrate hydrate in which R141b is the guest molecule is essentially the same as that for the formation of ice per mol of water. This property follows from the fact that clathrate hydrates are primarily hydrogen-bonded assemblies, analogous to water ice, and the van der Waals forces due to the guest molecule contributes relatively little energy to the structure, though these forces obviously have a critical effect on stability of hydrates. The value of the enthalpy change was confirmed experimentally by Liang [26], who determined the latent heat as 78.9 cal/gm (water basis), compared to 79.7 cal/gm for ice.

The assumption of adiabatic conditions was evaluated by conducting separate heating and cooling measurements in which no hydrate-forming guest molecules were present, although the contents of the cell were similar to the mass of liquids present during experiments, and the mixing characteristics were the same. Heating and cooling curves were generated from various temperature differences across the cell jacket, and the maximum heating and cooling rates determined by graphical analysis of the resulting temperature response data. The temperature of the coolant could be changed much more quickly than that of the cell contents due to the capacity of the thermostatic cooling apparatus and the limitations of heat transfer across the jacket wall, thus step changes in the coolant temperature could be used to observe the response of the material in the cell. In general, the cooling rates were much smaller than the rates at which the enthalpy change of hydrate formation generated sensible heat during the experiments. At relatively low hydrate formation rates, the appropriate correction for heat transfer through the cell jacket were added to the observed temperature change rate. The correction amounted to about 10% for the lowest rates measured but was much less for faster formation rates. Ignoring the heat capacity of the immersed metallic components of the hydrate cell causes the calculated rate data to slightly underestimate the true values by a few percent at most. As such, the rate data are somewhat conservative with regard to hydrate reactor design.

The kinetic data for R141b hydrate formation are plotted in Figure 7. The rate of incorporation of water into R141b hydrates are shown on the ordinate, in units of mol/sec, and the initial temperature is given by the x-axis. The data are grouped according to the initial saline concentration. The starting temperatures ranged from 1°C to 6°C and the saline concentrations from 0 to 7 wt.% NaCl. The rate of R41b hydrate formation was strongly dependent on temperature, so a logarithmic format was used to visualize the kinetic data. The functional dependence of the kinetics on temperature did not vary significantly according to the salinity, although the absolute values of the rates obviously did.

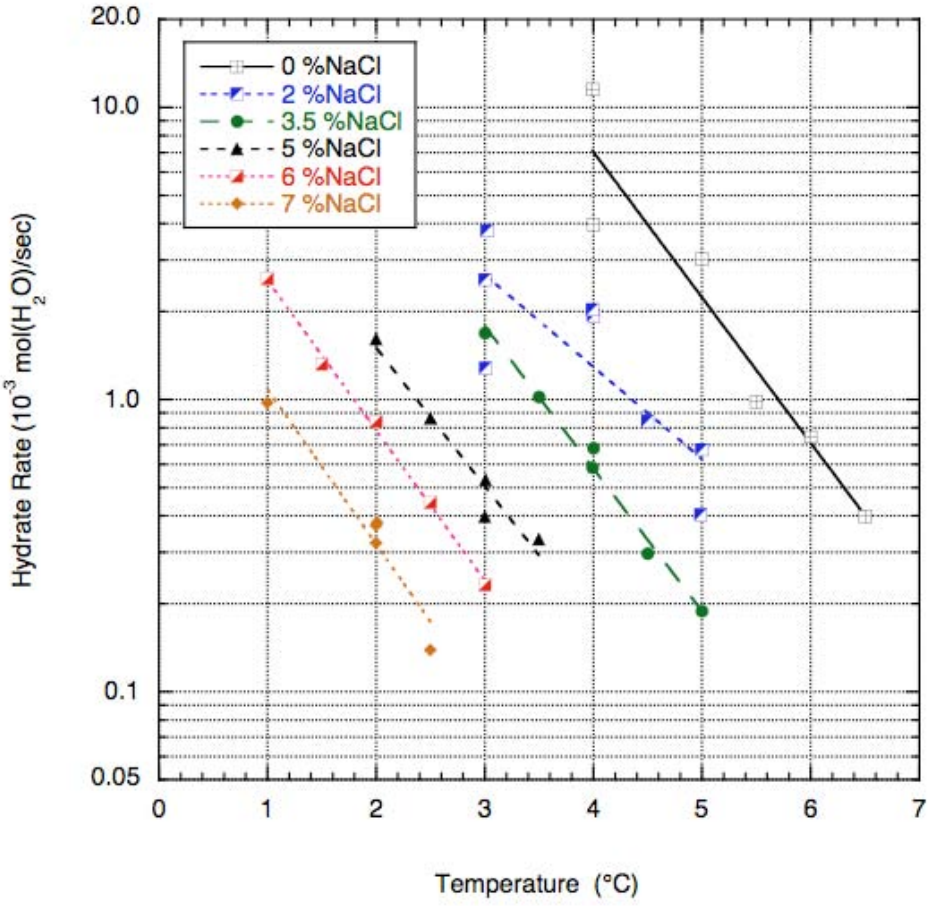

Figure 7. Rates of R141b clathrate hydrate formation in supercooled NaCl solutions vs. initial temperature and saline concentration. The hydrate formation rates are expressed as the rate of incorporation of water into the hydrate.

The rate data display the dependence on temperature and saline concentration that is expected intuitively. Relatively lower temperature produces faster rates of hydrate formation and relatively higher saline concentration slows the rate at a given temperature. The analysis of the kinetics of hydrate formation follows from the work of Barduhn concerning the crystallization of methyl bromide hydrate in seawater [27] as well as recent studies of the kinetics of methane hydrate formation.[28, 29] The primary driving force for hydrate crystallization is the degree of supercooling. The degree of supercooling for crystallization is simply the difference between the equilibrium temperature of a solid-liquid system and the temperature of the metastable material prior to solid formation. This same concept can be applied to hydrate formation if the relation between the critical stability (equilibrium) temperature and the saline concentration is quantified.

The effect of dissolved electrolytes, which do not form hydrates, on the critical stability temperature of clathrate hydrates has been analyzed by Engelzos [30] and Javanmardi [31], among others. This analysis had been applied to R152a hydrate formation by Kubota [32] and

Freon 21 hydrate formation by Barduhn [33], as these guest molecules are not soluble in water. Applying this approach for R141b, which is insoluble in water as well, the dependence of the equilibrium temperature (Teq) for R141b hydrate formation is analogous to the foregoing guest species, and the results are plotted in Figure 8. As an example, the equilibrium temperature for R141b hydrate formation is reduced from 8.4°C in deionized water to 5.2°C in 5 wt.% saline. The degree of supercooling, T, for a given experimental temperature and saline concentration can be simply calculated as T = T – Teq{NaCl concentration}.

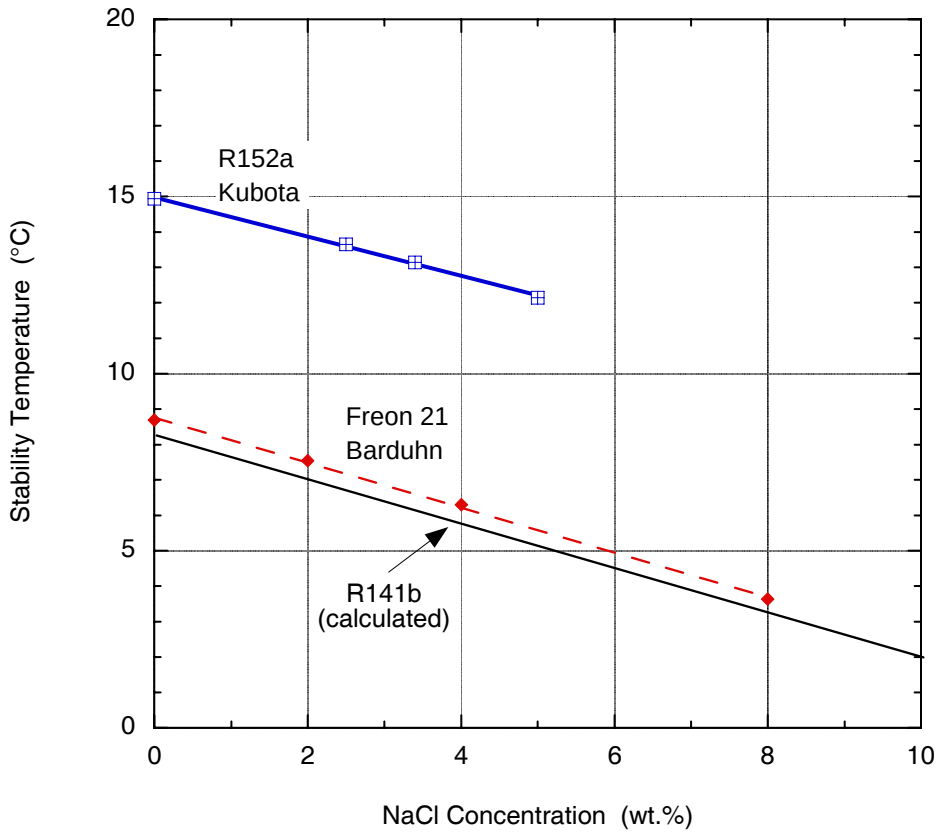

Figure 8. Depression of stability temperature of R141b hydrates according to saline concentration of aqueous solutions.

The kinetic data for R141b hydrate formation are plotted in Figure 9 using the degree of supercooling (T) as the x-axis variable. The same symbols are used to represent the data at various NaCl concentrations as used in Figure 7. All of the data basically collapse onto a single line (allowing for the variability of these experimental measurements) indicating that the supercooled state of the cell material is the key determinant of the rate of hydrate formation. Of course, this suite of rate data pertains specifically to the liquid-liquid phase contacting conditions that were maintained unchanged during the experiments. The rate data can be correlated with respect to T using a power-law equation as suggested by the linearity of the log-log plot; i.e. rate ~ T^p. The power-law exponent, p, was approximately 2.5 for the data shown. Pangborn

and Barduhn determined the rate of methyl bromide hydrate formation in saline water using a continuous flow stirred reactor and observed a power-law dependence on the degree of supercooling analogous to that reported here for R141b hydrates.[27] They argued that such a relatively large exponent implies that secondary nucleation was the controlling factor in hydrate growth, rather than extension of existing hydrate crystals. However, an investigation of the fundamental characteristics, such as the particle size distribution, that is important to a mechanistic analysis of the R141b hydrate growth process were beyond the scope of the current work. Regardless, the primary purpose of kinetic correlation developed here was to evaluate production scale possibilities and to provide a basis to compare the effect of a heat exchange fluid on hydrate formation and separation.

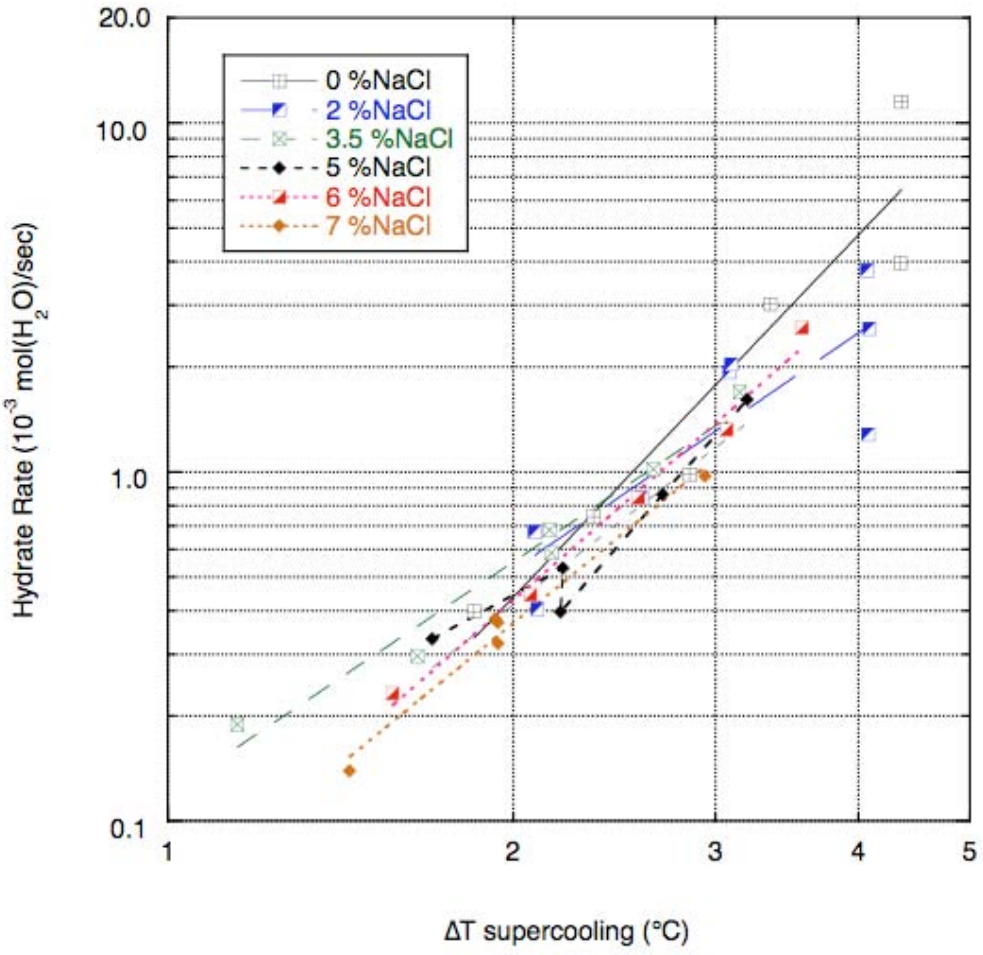

Figure 9. **Correlation of rate of R141b clathrate hydrate formation according to the degree of supercooling of saline solutions. The hydrate formation rates are expressed as the rate of consumption of water.**

The hydrate formation rates determined here are meaningful primarily as comparisons among the various conditions of temperature and salinity at which the rates were determined. The mixing characteristics of the multi-phase hydrate reactor used in the experiments reported here obviously will significantly affect the extrapolation of these data to other configurations, such as a much larger scale continuous stirred flow reactor that would be necessary for a practical desalination process. It should also be recognized that the present data do not necessarily represent optimal processing conditions and thus may be considered as a lower bound on rates that could be achieved. Regardless, an estimate of the rate of production of hydrates can be made from these data. For example, assume a hydrate reactor operates at 3°C and 5 wt.% NaCl (the inlet seawater concentration, 3.5 wt.% NaCl, must significantly increase within the reactor in a viable process scheme), which corresponds to a water uptake rate of 5.3×10^{-4} mol/sec according to Figure 7. The volume of the experimental reactor was approximately 200 mL. The per liter production rate is then 2.65×10^{-3} mol/sec/L. Given a desalination reactor volume of 1000 liters, a relatively modest size, the rate at which water is removed from the saline feed (for subsequent separation by decomposing the hydrate) is 2.65 mol/sec which corresponds to 1.8×10^{2} liter/hour. To a first approximation, such a production rate seems reasonable as the basis of a desalination process. Hydrate formation rates in a production-scale reactor would exceed those used in this example because the reactor would be operated so as to contain a significant amount of solid hydrates dispersed in the reaction media. These hydrates would serve as secondary nucleation sites and thereby drive further hydrate formation.

The typical appearance of R141b hydrates is shown by the photographs of material in the reactor cell in Figure 10. These particular experiments were conducted using 2 wt.% NaCl solutions at 5°C and 1°C, respectively. The hydrate mass was observed at the surface of the saline solution, indicating that its density is somewhat less than water. The hydrates tended to clump together rather than being easily dispersed in the absence of the agitation used during the formation period. The unhydrated R141b (not visible in photographs) forms a liquid layer at the bottom of the cell due to its immiscibility with water and its greater density. The appearance of the hydrates suggests that the material can be physically separated from the residual brine although a key parameter for desalination is the extent to which the hydrate mass has brine entrapped within the aggregate, which will contaminate the water recovered after the hydrate has been melted.

Figure 10. **(Upper) R141b hydrate slush formed by 2 wt.% NaCl solution at 5°C in a stirred batch reactor. The elapsed time for this experiment was approximately 1000 seconds. (Lower) Appearance of R141b clathrate hydrates formed at 1°C in 2 wt.% NaCl solution.**

This page has been intentionally left blank

4. R141b Hydrate Formation - Effect of a Heat Exchange Fluid

The efficacy of the heat exchange fluid technique for controlled formation and separation of clathrate hydrates was investigated using the combination of R141b as the guest molecule and Fluorinert as the heat exchange fluid. The particular Fluorinert chosen was FC3283, a mixture of perfluorocarbons having an average molecular weight of 571 and low volatility at the temperatures of interest for desalination. FC3283 also has excellent heat transport properties, as befits its primary commercial application as a coolant for electronics. Despite regulatory restrictions concerning HCFC materials, R141b is a useful starting point to explore the heat exchange fluid method in general. An understanding of R141b hydrate formation behavior in the presence of a heat exchange fluid will aid process development based on other liquid-phase hydrate guest molecules, including cyclopentane and fluorocyclopentane, among numerous others.

Growth rate studies involving a liquid guest molecule are also relevant to other guests that are ordinarily gases at ambient temperature but have sufficiently low vapor pressure such that condensation will occur when the guest is introduced into the reactor at moderate pressure. Examples of such guest molecules include difluoromethane and difluoroethane, among a variety of HFC molecules that form hydrates at relatively high temperatures.[25] Other guest-heat exchange fluid combinations that can be envisioned include any relatively small hydrocarbons that form either sI or sII hydrates at moderate pressures, such as ethylene, propane, cyclopropane, etc. These hydrocarbons would create systems in which the guest molecule and heat exchange fluid are miscible, if inert hydrocarbons of higher molecular weight were used as the heat exchange fluid. If a liquid such as Fluorinert is used with a hydrocarbon guest molecule, an immiscible guest-heat exchange fluid combination results. The scope of this project focused on studying some aspects of the behavior of a miscible combination.

To assess the effect of a heat transfer fluid on the rate of hydrate formation and the type of macroscopic hydrate aggregation, a matrix of experiments was conducted using mixtures of R141b and Fluorinert FC3283, which are completely miscible with each other but immiscible with the aqueous phase. In this matrix, saline concentration varied from 0-7 wt.% NaCl, initial temperatures were varied between 1°C to 6°C, and hydrate growth was initiated by secondary nucleation as with R141b only. The mol fraction of R41b in Fluorinert was kept constant at 0.33 (equivalent to 10 wt.%) for most experiments, although a separate series was conducted using a mol fraction of 0.4 to observe the effect of R141b concentration on hydrate formation. A total of 41 experiments with R141b and Fluorinert FC3283 were performed including several replicates. Separation behavior of hydrates from brine was determined in some of these experiments.

The same data analysis procedure described in the preceding section for pure R141b was applied to evaluate the effect of a heat exchange fluid on R141b hydrate growth. Rate data were extracted from measurements of the temperature of the hydrate-liquid-liquid slurry in the reactor to the time of growth of hydrate material. The temperature-time profile of a typical R141b-Fluorinert hydrate experiment is shown in Figure 11. The temperature was measured at two

locations in the slurry and both thermocouples ordinarily displayed the same rate of temperature increase as shown in the graph. The time course followed a very repeatable pattern that mimicked the observations from R141b experiments. At the outset of hydrate growth, the temperature gradually increased as hydrate formation was stimulated by secondary nucleation due to the addition of R141b seed material. Following this acceleration period, a linear temperature ramp was observed which typically persisted for a significant portion of the hydrate growth phase. The rate of temperature increase then decelerated and reached a plateau that was usually limited by the equilibrium temperature for hydrate formation rather than the amount of one of the hydrate-forming species.

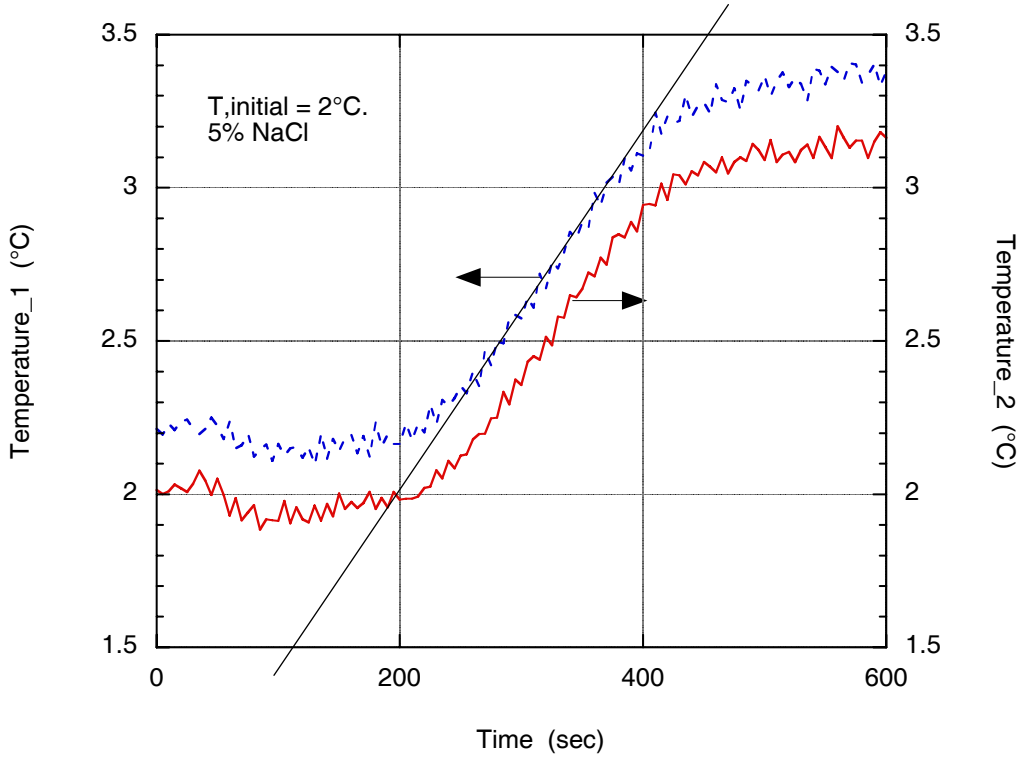

Figure 11. **Temperature-time profiles in a stirred batch reactor during R141b clathrate hydrate formation in the presence of Fluorinert FC3283. The aqueous phase was 5% saline solution at an initial temperature of 2°C. The temperature at two locations in the R141b-hydrate-saline slurry are given by the left and right ordinates. The offset is due to the characteristics of the individual thermocouples. The straight line superimposed on the curves indicates the linear section of the temperature-time profiles that was used to calculate the apparent rate of hydrate formation. Both thermocouples displayed the same rate of temperature increase.**

The linear portion of the temperature-time profile is common to every kinetic experiment in which R141b hydrates were formed in the R141b-Fluorinert mixture. This linear growth period

provided the basis for comparing rate data from the matrix of experiments conducted at various dissolved salt concentrations and initial temperatures. The straight line in Figure 11 indicates the linear section of the temperature-time profiles that was used to calculate the apparent rate of hydrate formation for the representative experiment shown. The same equation (Equation 1) described in the preceding section of the report was used except that the mass and heat capacity of FC3283 was included in the calculation.

The kinetic data for R141b hydrate formation with Fluorinert are plotted in Figure 12 for mixtures in which the mol fraction of dissolved R141b was 0.33. The rate of incorporation of water into R141b hydrates are shown on the ordinate, in units of mol/sec, and the initial temperature is given by the x-axis. The data are grouped according to the saline concentration. The starting temperatures ranged from 1°C to 6°C and the saline concentrations from 0 to 7 wt.% NaCl. The rate of R41b hydrate formation was strongly dependent on temperature, so a logarithmic format was used to visualize the kinetic data. Compared to pure R141b, the rate of hydrate formation with Fluorinert was reduced by a factor of 3 to 4. This reduction corresponds roughly to the mol fraction of R141b in the mixture. Another source of variation concerns mixing. Although mixing parameters (impeller type and position, rotational speed, liquid phase levels) were kept constant and duplicated R141b experiments as closely as possible, subtle changes in the dispersion characteristics of the liquid-liquid phases, and thereby the interfacial contact area, may have occurred. The viscosity and density of the R141b-Fluorinert mixture are greater than pure R141b, and thus the fluid mechanical response to agitation may have systematically varied.

The rate data display the dependence on temperature and saline concentration that was observed for R141b alone. Relatively lower temperature produces faster rates of hydrate formation and relatively higher saline concentration slows the rate at a given temperature. The analysis of the kinetics of hydrate formation follows from the preceding section. The conditions of temperature and salinity were used to transform the data according to the degree of supercooling. The kinetic data for R141b hydrate formation with Fluorinert are plotted in Figure 13 using the degree of supercooling (T) as the x-axis variable. The same symbols are used to represent the data at various NaCl concentrations as used in Figure 12. In the present case, the kinetic data do not collapse onto a single line as for pure R141b. This behavior indicates that although the supercooled state of the cell material is the key determinant of the rate of hydrate formation, other factors also influence the rates. The rate data can be correlated with respect to T using a power-law equation as suggested by the linearity of the log-log plot; i.e. rate ~ T^p. The power-law exponent, p, was approximately 5 for the data shown. Pangborn and Barduhn determined the rate of methyl bromide hydrate formation in saline water using a continuous flow stirred reactor and observed a power-law dependence on the degree of supercooling analogous to that reported here for R141b hydrates.[27] They argue that such a relatively large exponent implies that secondary nucleation is the controlling factor in hydrate growth, rather than growth of existing hydrate crystals. However, an investigation of the fundamental characteristics, such as the particle size distribution, that are important to a mechanistic analysis of the R141b hydrate growth process is beyond the scope of the current work. Regardless, the primary purpose of kinetic correlation developed here is to evaluate production scale possibilities and to provide a basis to compare the effect of a heat exchange fluid on hydrate formation and separation.

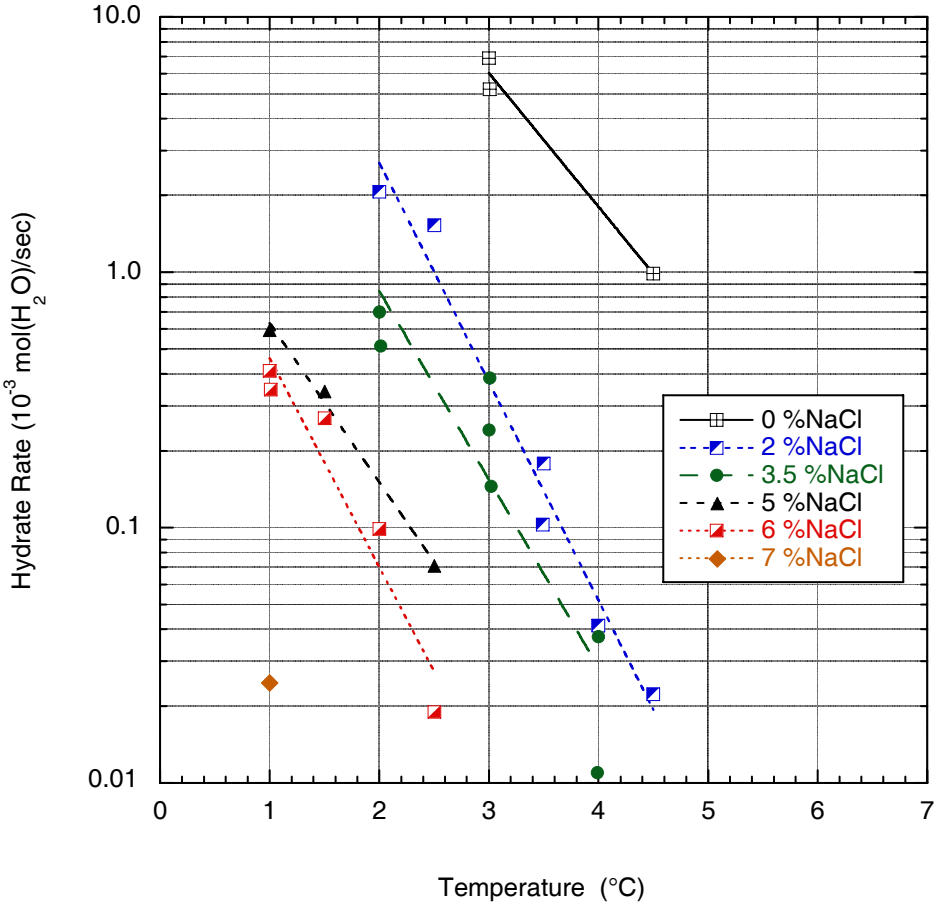

Figure 12. **Rates of R141b clathrate hydrate formation in supercooled saline solutions vs. initial temperature when R141b was dissolved in the heat exchange fluid, Fluorinert FC3283, for mole fraction of 0.33 R141b. The data are grouped according to the saline concentration. The hydrate formation rates are expressed as the rate of consumption of water.**

The rate data are well correlated by the same exponential functional dependence on the degree of supercooling of the saline solution. However, the rates also depend explicitly on the saline concentration, as shown in Figure 13. This latter effect may be due to the dispersion characteristics of the R141b-Fluorinert mixture in saline. Regardless, the results demonstrate that hydrate rates are well within a range that implies realistic scale-up to a production system.

A possible reason that the hydrate formation rate data for mixtures of R141b with Fluorinert FC3283 do not collapse to a single line, as the data does for R141b alone, is that the morphology of the hydrates formed is different. While R141b alone forms aggregated solids, the mixture formed hydrate-covered droplets in most instances. The droplets are more dense than pure R141b, as noted in the Experimental section of this report, and probably mix differently in the

cell. Thus, different growth rates could occur depending on mixing parameters alone. In some cases, differences in the mol fractions of dissolved R141b may be the cause as well.

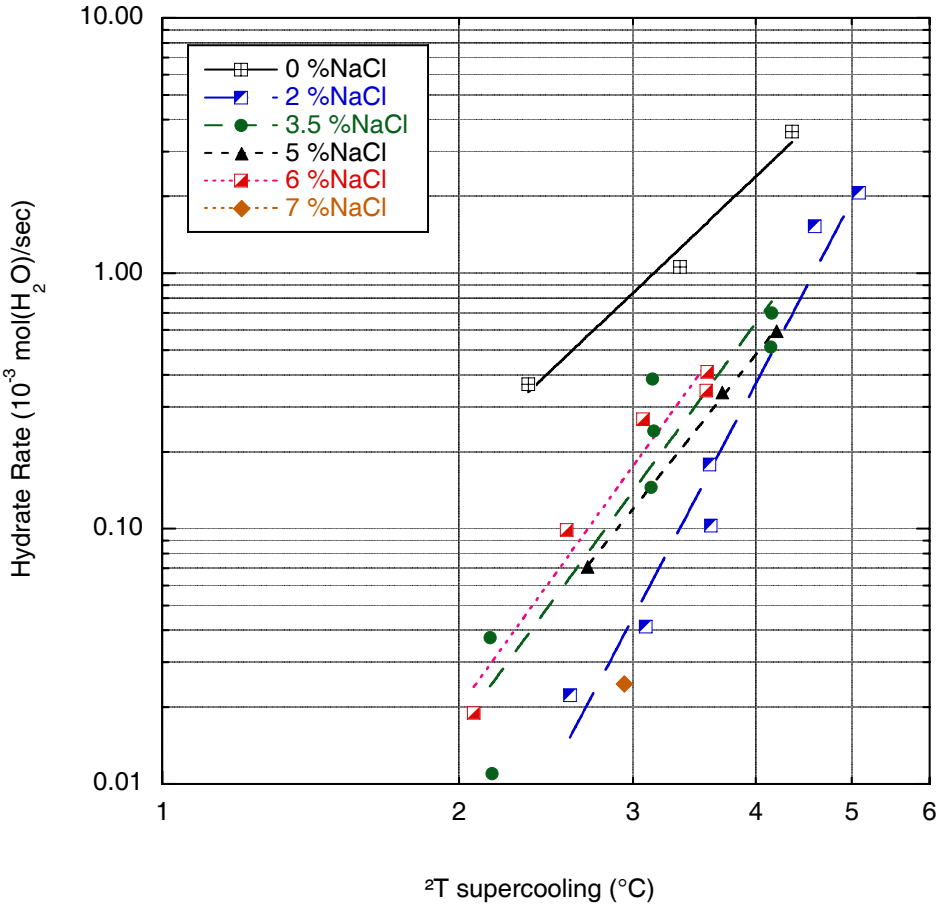

Figure 13. Correlation of rates of R141b clathrate hydrate formation according to the degree of supercooling of saline solutions when R141b was dissolved in the heat exchange fluid, Fluorinert FC3283. The hydrate formation rates are expressed as the rate of consumption of water.

The effect of the concentration of R141b dissolved in the heat transfer fluid was investigated in a series of experiments. R141b-Fluorinert mixtures containing a mol fraction of R141b of 0.4 (corresponding to 13 wt.%) were prepared and hydrate growth experiments conducted using saline concentrations of 0, 2 and 5 wt% NaCl. The results of the rate measurements are plotted in Figure 14. The rates depend directly on the mol fraction of R141b with those for values of 0.4 being distinctly greater than those for 0.33. However, it is apparent from the data that the dependence on the temperature, and thus degree of supercooling, follows the same relationship regardless of the concentration of R141b. These results imply that the concentration can be varied to achieve acceptable hydrate formation rates and separation.

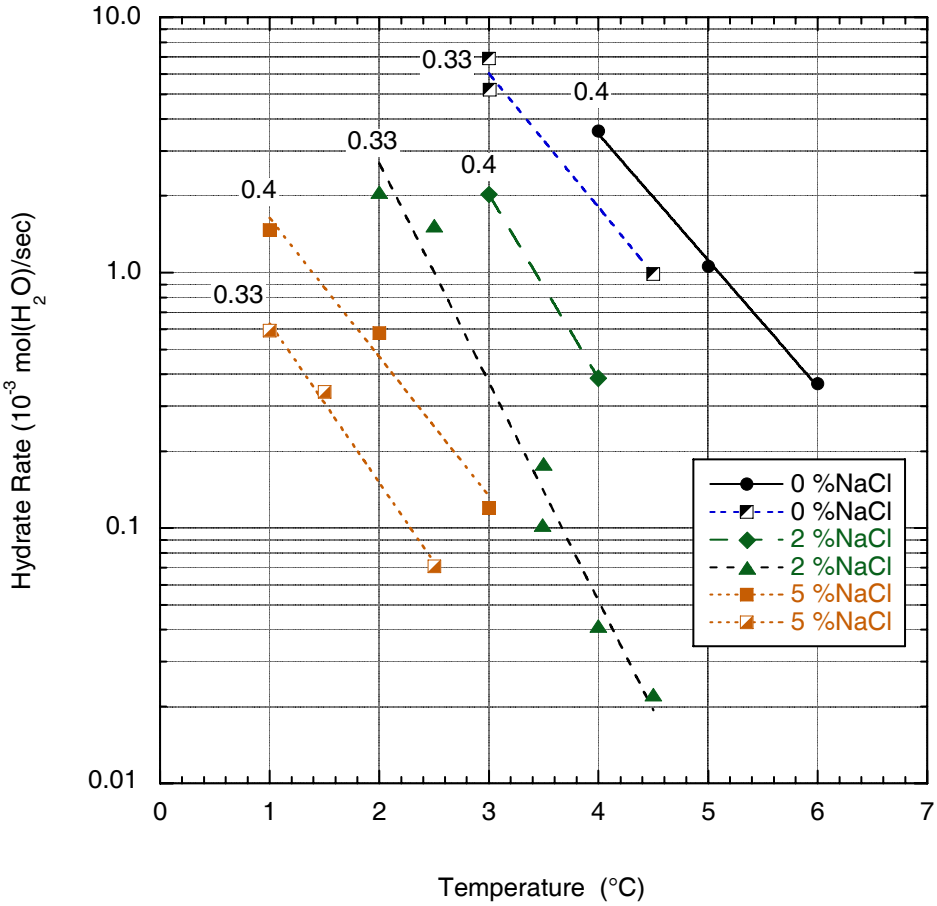

Figure 14. Effect of proportions of R141b dissolved in Fluorinert on rates of R141b clathrate hydrate formation. The rates are given for several supercooled saline solutions vs. initial temperature for mol fractions of R141b of either 0.33, 0.45 or 1.0 (R141b alone). The data are grouped according to the saline concentration. The hydrate formation rates are expressed as the rate of consumption of water.

The typical appearance of R141b hydrates formed in the presence of Fluorinert is shown by the photographs of material in the reactor cell in Figure 15. These particular experiments were conducted at in 5 wt.% NaCl at 3°C (upper) and 1.5°C (lower). The morphology is distinctly different than with R141b alone. The hydrate was formed primarily as a coating of the solid material on droplets of the R141b-Fluorinert mixture. These dispersed droplets were physically stable after agitation ceased and settled to the bottom of the cell because the density of the organic fluid mixture was 1.36 gm/cm^3, much higher than saline. Residual R141b-Fluorinert mixture formed a liquid layer at the bottom of the cell. The appearance of the hydrate-covered droplets suggests that the material can be physically separated from the residual brine by simple sedimentation methods. A key parameter for desalination, however, is the extent to which the hydrate dispersion contains entrapped brine, which will contaminate the water recovered after the hydrate has been melted.

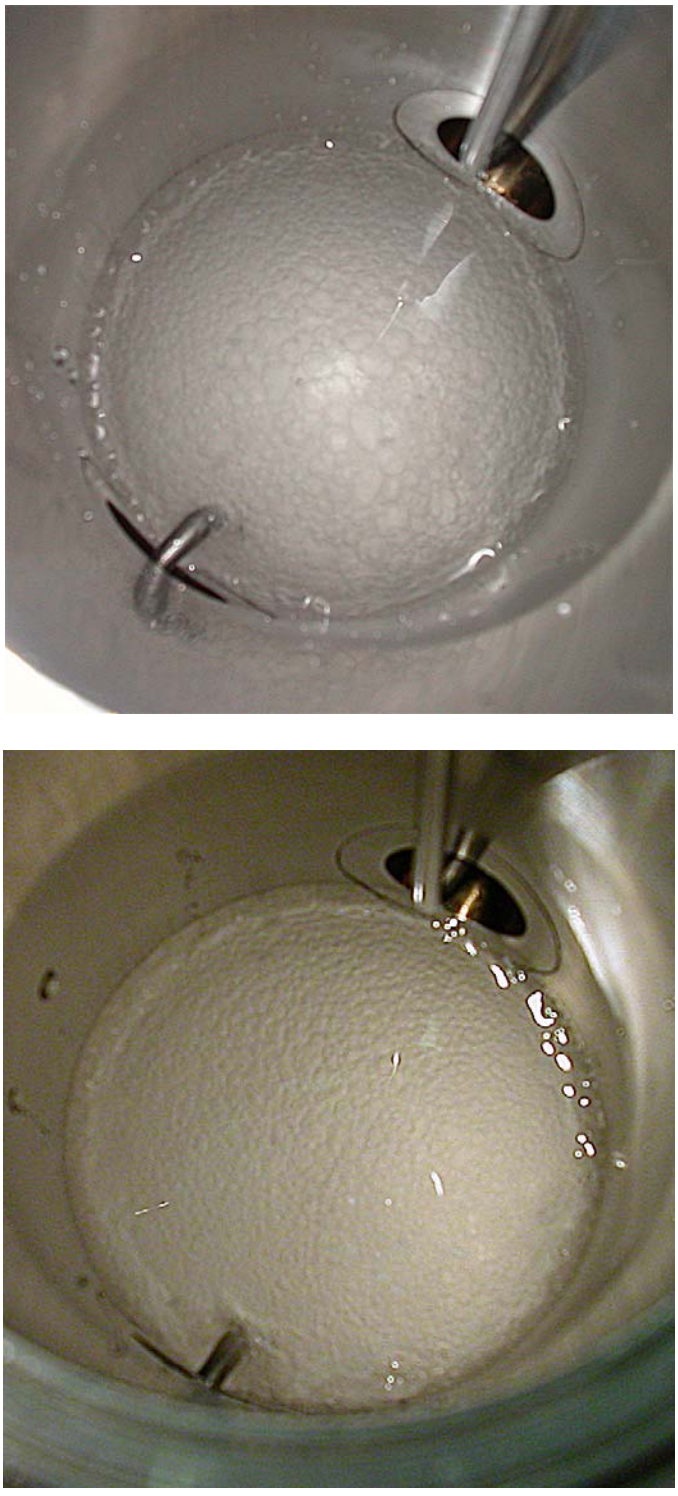

Figure 15. **Hydrates formed by R141b dissolved in Fluorinert 3283 produced hydrate-coated droplets that were more dense than water. These experiments were conducted in 5 wt.% saline at 3°C (upper) during an elapsed time of about 800 sec. and at 1.5°C (lower) for approximately 600 sec.**

Table 1 presents data from a group of R141b-clathrate hydrate experiments in which separation of water from saline water was demonstrated. In these experiments the hydrate-forming compound, R141b was dissolved in Fluorinert at the concentration indicated in the table. Two test cell configurations were used, either stirring approximately equal amounts of an aqueous saline solution and the R141b-FC3823 mixture or injecting the saline solution into a body of agitated R141b-FC3823 mixture. The salinity of the aqueous solutions charged to the test were measured by refractive index before and after the formation of hydrates The data show that the saline solution became concentrated as water was removed by the formation of the clathrate hydrate. In one case, hydrate material was recovered after the test and melted, whereupon the aqueous phase separated spontaneously from the immiscible organic liquid and its salinity was determined.

Table 1. Salinity of NaCl solutions before and after R141b hydrate formation in a mixture of R141b and Fluorinert FC3283.

Temp.	R141b	NaCl	NaCl	NaCl
°C	wt%	wt%	wt%	wt%
		Initial	Final	Melted
				Hydrate
3	25	2.64	2.95	
3	25	3.69	4.43	
3	25	2.51	2.83	0.50
3	25	2.25	2.49	
2	14	6.49	7.63	
2	11	4.87	5.60	
3 (a)	19	4.72	5.35	
4 (a)	19	1.83	2.27	

(a). The saline solution was injected into the stirred R141b-Fluorinert mixture rather than initiating hydrate formation from stirred immiscible layers of approximately equal proportions.

These experiments demonstrate that the approach of using an inert heat transfer fluid produces a significant separation of water from saline solutions. The heat transfer fluid technique to facilitate the separation of the hydrate material is likely to be generally applicable to a variety of prospective hydrate forming agents. A heat exchange fluid may serve another useful purpose downstream of the hydrate reactor when the hydrate material is decomposed to recover desalted water and the guest molecule. The water spontaneously separates from the liquid phase containing the heat exchange fluid and its soluble guest molecules. The design of a heat transfer equipment for the decomposition process step will be simplified and more efficient if the hydrate can be conveyed to the device as a mixture of hydrate-coated droplets rather than moving a “wet cake” of solid hydrate material.

5. Molecular Dynamics Simulations of Hydrates

5.4 Introduction

Clathrate compounds consist of a solid framework of host molecules that surround guest molecules. The term clathrate hydrate applies when water is the host molecule and are characterized by forming conditions of temperature 0°C and pressure 1 atm.[34] Structure I hydrates consist of two types of water cages: a small cage consisting of 20 water molecules and denoted 5^{12}, and a large cage consisting of 24 water molecules, ($5^{12}6^2$). Structure II hydrates also have the 20-water small cages as well as large 28-water cages ($5^{12}6^4$). In both structure I and structure II hydrates, water molecules maintain tetrahedral coordination through four hydrogen bonds per molecule, as in hexagonal ice. The molecular diameter of a guest molecule determines the appropriate cage and therefore the type of hydrate formed.[c1] Clathrate hydrates consisting of natural gas guest molecules (e.g., methane) have received attention as a potential energy source, although pressures greater than 20 atm and temperatures near 273 K are required for hydrate stability.[35]

Clathrate hydrates can form in the presence of dissolved solutes and therefore have potential use in water desalination processes. Guest molecules considered for this application have included propane [36] and chlorofluorocarbons.[37,38] However, many complex and fundamental issues remain to be solved before hydrate desalination can be considered as a commercial technology. Specifically, hydrate nucleation, growth, and crystal agglomeration must be understood. In the presence of dissolved solute, trapped solute and recovery of pure water from a hydrate phase must also be considered. Using computational and spectroscopic techniques, our aim is to characterize guest-water interactions at the molecular level to aid in understanding the more complex issues associated with the hydrate desalination process.

Experimental studies of the structure and phase equilibria of gas hydrates formed by chlorofluorocarbons and other large guest molecules have been reviewed elsewhere.[34,39-42] Raman spectroscopic techniques have been used recently to better understand guest-host interactions at the molecular level.[43-45] Comparisons between spectroscopic and computational techniques will enable more effective use of gas hydrates in industrial applications. Computational studies of gas hydrates typically include as guest molecules either methane [46-58] or hydrogen [54, 59, 60] because of their potential use in energy storage and production. Typically, the guest is treated as a single Lennard-Jones particle, [50, 52, 53, 55-57, 61] although atomistic models for both [46,47] and hydrogen [59, 60] have been published. In some cases, *ab initio* calculations have been performed, and guest-water interaction parameters were derived for classical simulations. [51,53,61,62] Simulation techniques have also been used to study the thermodynamics of hydrate formation and dissociation, although simulation time scales of at least 10 ns are typically needed, [52,55,56,58] and effects of finite system sizes should also be considered. [47]

The classical simulation approach used in this study follows from previous work in which a general force field for organics (Consistent Valence Force Field, CVFF) [63] was used to

calculate thermal expansion parameters and vibrational spectra of methane hydrate. [49] The advantage of a general force field is its transferability to new hydrate systems without the need to derive new water-guest interaction parameters. In this report, we use molecular simulation techniques to examine the structure and stability of gas hydrates formed from two isomers of dichlorofluoroethanes. One of these isomers 1,1-dichloro-1-fluoroethane (R141b, **1** in Figure 16), is being considered as a hydrate former in water desalination processes. [64] Its high heat capacity and mild hydrate forming conditions (8°C, 75 mbar) make R141b an ideal candidate for low-energy water desalination.[39] Additionally, we compare simulated vibrational spectra with Raman spectra to investigate changes in R141b vibrational frequencies before and after formation of the hydrate phase. United States law now prohibits the production or importation of R141b, but we chose it based on the availability of experimental data on R141b hydrates. [39,41,65-67] Industrial applications of hydrates made from trihaloethanes will include refrigerants that are allowed under current law.

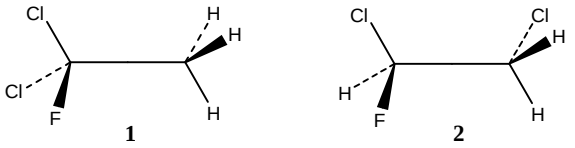

Figure 16. Hydrate formers considered in this work: 1 (1,1-dichloro-1-fluoroethane, R141b) and 2 (1,2-dichloro-1-fluoroethane).

5.4 Methods

Due to their size, dichlorofluorohaloethanes form structure II hydrates, where we assume an occupancy of one molecule in each of the 8 large cages. The 16 small cages are empty in the pure hydrate, but smaller guest molecules such as methane could be included in the small cages. Cavity diameters for accommodation of guest molecules have been estimated at 6.7 Å and 5.0 Å for the large and small cages, respectively.[34]

5.2.1 Density Functional Theory (DFT) Methods

Electronic structure calculations for cluster models of the structure II large ($5^{12}6^4$) and small (5^{12}) hydrate cavities with the R141b molecule were completed using the density functional code DMol^3.[68,69] Structural models for each cavity were taken from the experimental data of a mixed gas hydrate (structure II, space group *Fd*3*m*, *a* = 17.192 Å) with Xe atoms occupying the small cages and CCl_4 molecules occupying the large cages. [70] This lattice parameter is very close to 17.234 Å reported for R141b hydrate.[6] Because atomic coordinates were not reported in ref 6, we chose to use both the coordinates and lattice parameter of another structure II hydrate. [70] We are confident that 17.192 Å is an adequate estimate of the R141b hydrate lattice parameter for the DFT calculations. Hydrogen positions of the water molecules were classically optimized as described below. All-electron configurations were obtained for the geometry-optimized R141b molecule within each hydrate cavity with fixed positions for the water molecules. Similar calculations were performed for the isomer (1,2-dichloro-1-fluroethane, **2** in

Figure 17; *gauche* and *anti* configurations) to determine the relative energies and suitability as a hydrate-forming compound. Calculations incorporated the nonlocal gradient-corrected or generalized gradient approximation, with double numerical plus polarization functionals to ensure a proper description of the hydrogen bonding for the water and organic molecules.[71] Iteration of the wave equations to a self-consistent field solution required an energy difference of less than 0.0063 kJ·mol^{-1}. Energy-minimized structures were derived through a series of steepest descent, conjugate gradient, and Newton-Raphson methods allowing all atoms to relax during the optimization. An energy convergence criteria of 0.013 kJ·mol^{-1} was used for the geometry optimization of the dichlorofluoroethane while keeping the water molecules constrained to their observed structural positions.

A similar computational approach was used to examine the electronic structure of crystalline models of the R141b hydrate and isomer hydrate systems. The periodic simulation cells were equivalent to the isometric structure II unit cell with 136 water molecules, eight dichlorofluoroethane molecules occupying the large cavity, and vacant small cavities. Wavefunctions were calculated using a single integration in reciprocal space (gamma point). The cell parameter (a_o=17.192 Å) was held constant for constant volume conditions during the optimization, and no symmetry was imposed on the atomic positions (*P*1 space group). In contrast to the cluster calculations, all atomic positions were relaxed during the optimization of the periodic models.

Vibrational spectra for the cluster models of R141b and R141b hydrate were derived using the standard approach of Wilson [72] in which the components of the second derivative of the energy (Hessian matrix **F**) are used to derive harmonic frequencies,

$$\mathbf{F}_{ij} = \frac{1}{\sqrt{m_i m_j}} \frac{\partial^2 E}{\partial q_i \partial q_j} \tag{2}$$

where m_i and m_j are atomic masses and q_i and q_j are Cartesian coordinates associated with atoms i and j. The frequencies are equivalent to the square roots of the eigenvalues of **F**. Finite differences of the analytical first derivatives of the energy are used to derive the Hessian matrix. This solution is accomplished by a series of single point energies that are obtained as each atom in the system is displaced by 0.01 Bohr in each direction. Spectral intensities for each mode are proportional to the square of the atomic polar tensor. Lorentzian-shaped peaks with 5.0 cm^{-1} full width at half maximum were derived from the calculated frequencies. No attempt was made to derive vibrational spectra for the crystalline models using this method because of computational cost. The calculated vibrational spectra involving the hydrate cavity are also only approximate representations of the cluster dynamics because the water molecule positions were constrained to best represent the local water cavity structure. Power spectra derived from velocity autocorrelation methods with classical simulations are closely related to the spectra obtained through the Hessian analysis of electronic structure results. Classical methods rely on kinetic energy to statistically sample accessible regions of the potential energy surface over long simulation times at a particular temperature, while the dynamical matrix in normal model analysis directly samples the electronic-based internal energy surface at 0 K.

5.2.2 Classical Molecular Dynamics

Classical simulations were performed with the Open Force Field module of Cerius^2 (Accelrys, Inc.) using the Consistent Valence Force Field (CVFF).[63]. Intermolecular potential parameters between organic guest atoms (C, H) and host water molecules (Simple Point Charge model [73]) were obtained from geometric combination rules upon which CVFF is based. CVFF has previously been shown to provide accurate structural results for methane hydrate,[49] and here we apply similar techniques to more complex trihaloethane guests. Because CVFF includes molecular flexibility for both water and guest molecules, we were able to calculate vibrational power spectra from atomic velocity autocorrelation functions.[74] Potential energy interactions included intramolecular (bond, angle, torsion) as well as intermolecular (electrostatic, van der Waals) terms. A real-space cutoff value of 10.0 Å was used for intermolecular interactions and Ewald summation [74] with a precision of 4×10^{-4} kJ·mol^{-1} was used for long-range electrostatic interactions. Initial simulations were performed in the constant *NPT* (*N* = number of particles, *P* = 0 atm pressure, *T* = temperature) ensemble to obtain average supercell volume and lattice parameters. Subsequent simulations to obtain structural and vibrational data were preformed in the constant *NVT* (*V* = volume) ensemble using an equilibrated *NPT* configuration with lattice parameters equal to their average values at that temperature. Barostat and thermostat relaxation times were 0.5 ps and 0.1 ps, respectively. All force field parameters, including atomic charges, were taken directly from CVFF.[63] The timestep for all simulations was 0.25 fs.

Our primary interest is R141b hydrate, **1**, but in order to examine the effect of molecular size on hydrate stability, we also considered isomer, **2**. For the computational portion of this study, we only considered the *S*-enantiomer of **2**. Due to the symmetry of the water cage, we would not expect different structural or vibrational results if we had used the *R*-enantiomer. The initial configuration of water O atoms was the same as that used for the DFT calculations. The initial positions of H atoms were determined by a series of energy minimizations with immobile O atoms, which resulted in a hydrogen-bonded network of water cages. Although the unit cell dipole moment is not zero in our initial configuration, the Bernal-Fowler rules [75] are satisfied. Macroscopic system sizes would be needed to obtain a dipole moment of zero, and the thermal energy at the temperatures used in our Molecular Dynamics simulations causes the net dipole moment to fluctuate. In fact, we observe rotations of water molecules during these simulations, which cause a cascade effect of hydrogen bond breaking and re-forming and associated changes in the dipole moment. A supercell was created consisting of 8 unit cells in a 2 x 2 x 2 expansion, with an initial lattice parameter of 34.384 Å. The supercell contained 1088 water molecules, 64 large cages, each occupied by a trihaloethane (**1** or **2**), and 128 empty small cages. The trihaloethane molecules were placed randomly within the large cages while avoiding overlap of atomic van der Waals radii.

The temperature ranges of stable hydrates were determined by performing anisotropic *NPT* simulations of 1000 ps in length. R141b hydrate was stable at temperatures up to 265 K. Above 265 K, the hydrate system dissociated into an aqueous phase and an organic phase. The isomer hydrate was stable only at temperatures below 150 K. Because periodic models of solids lack a surface nucleation site, solid phases such as ice can be stable at temperatures well above the simulated melting temperature.[78] Therefore, 265 K and 150 K should be considered as upper limits for the thermal stability of hydrates with guests **1** and **2**, respectively. We have not found a published melting temperature of ice Ih using the flexible SPC water model, but the simulated

melting temperatures of Ice Ih using the rigid SPC and SPC/E water models have been reported as 190 K and 215 K, respectively.[77] Using the SPC/E water model, ice Ih was found to be stable in *NPT* Monte Carlo simulations up to 295 K, which is 80 K above its transition temperature.[76] It is therefore likely that the simulated dissociation temperatures for hydrates of **1** and **2** using our hybrid force field are significantly lower that 265 K and 150 K. However, based on our desire to match the theoretical and experimental conditions, further simulations were carried out in the *NVT* ensemble with T = 265 K. The initial configuration was taken from the equilibrated *NPT* configuration of R141b hydrate at 265 K. Lattice parameters (**a**, **b**, **c**) were 34.28 Å, 34.54 Å, and 33.92 Å, respectively, which correspond to average values from the *NPT* simulation at 265 K. One set of simulations were performed in which the waters were completely mobile. Because the isomer hydrate is not stable at 265 K, however, a second set of simulations were performed in which the water molecules were held in fixed positions based on their initial configuration. In this way, comparisons were made between hydrates of both **1** and **2**. Initially, *NVT* simulations of 40 ps in length were used to obtain structure and vibrational data, but longer simulations of 1000 ps in length were used to further investigate guest rotational mobility within the cages. For the 40-ps simulations, RDF data were updated every 50 fs, and velocities were stored every 4 fs. Power spectra of R141b hydrate (mobile water molecules) were obtained by taking the Fourier transform of the velocity autocorrelation functions (VACFs) for each atom type. A VACF window of 20 fs was used, which was also used to obtain power spectra of methane hydrate.[49] For comparison, power spectra were also obtained from 40-ps *NVT* simulations of hexagonal ice and pure R141b at 265 K. For Ice Ih, the supercell contained 360 molecules. The model system for pure R141b corresponded to a pressure of 300 kbar at 265 K (120 molecules in a cubic supercell of dimension 20.0 Å).

5.2.3 Hydrate Synthesis and Characterization

A stirred thermostatic pressure cell was used to synthesize R141b (CAS 1717-00-6) hydrate, as described elsewhere.[64] Hydrate samples were prepared at approximately 3°C and atmospheric (total) pressure using R141b-hydrate seed crystals, prepared separately by flash freezing, to facilitate rapid hydrate growth. Attempts to make hydrate samples of the isomer (CAS 430-57-9) (**2**) were unsuccessful. Approximately a gram of the isomer was placed in test tubes along with 5 mL of water. Trials were conducted simultaneously with homogeneous nucleation and secondary nucleation using a few mg of R141b-hydrate seed crystals. Comparable tubes with R141b were prepared as controls. The test tubes were placed in a refrigerator for at least 3 days at 3°C and periodically agitated. No hydrate phase was observed for the isomer, although R141b hydrates were formed. The temperature was subsequently reduced to just above 0°C but no hydrates of the isomer were detected. Raman spectra were collected using an Acton (Princeton Instruments) 0.75m SpectraPro 2750 triple grating spectrograph, with the 532 nm line from a Spectra-Physics Excelsior CW diode-pumped Nd:YAG. Collection times for the clathrate and the R141b reference were 10s, and 1s, respectively, with a power at the sample of approximately 10mW. Clathrate samples and the R141b reference were held at approximately 0°C on a thermoelectric cold plate during data collection. The spectra were calibrated using a 20 point neon spectrum. Data were fitted for peak locations with pseudo-Voigt and/or Gaussian peak shapes, using FITYK 0.7.5 (www.unipress.waw.pl/fityk).

5.2.4 DFT Methods

A comparison of the energies obtained from the DFT calculations for the various clathrate systems is presented in Table 1. Due to the difficulty in DFT methods in reproducing dispersion-related effects in intermolecular systems, caution must be used in interpreting the results of the optimized cluster and periodic systems. Results from the cluster models demonstrate the size restrictions associated with the incorporation of R141b or other similarly-sized guest molecule in the small hydrate cavity. The formation energy for R141b in the optimized large water cavity—presented here relative to the water cavity structure—indicates a stability of -209 $kJ \cdot mol^{-1}$ in contrast to +161 $kJ \cdot mol^{-1}$ for R141b in the small cavity.

Table 2. Energies of water, guests, and clathrates derived from DFT.

	Number of H_2O molecules	**Potential E** ($kJ \cdot mol^{-1}$)	**E_{form}** ($kJ \cdot mol^{-1}$)
Cluster models			
Water molecule	1	-200682	
R141b		-2883584	
1,2-dichloro-1-fluroethane (gauche)		-2883573	
1,2-dichloro-1-fluroethane (anti)		-2883577	
Small cavity	20	-4014219	
Large cavity	28	-5619886	
R141b in small cavity	20	-6897642	+161
R141b in large cavity	28	-8503679	-209
Isomer in large cavity (gauche)	28	-8503661	-201
Isomer in large cavity (anti)	28	-8503646	-184
Periodic models			
R141b in large cavity	136	-50371742	-4743
Isomer in large cavity (gauche)	136	-50371594	-4682

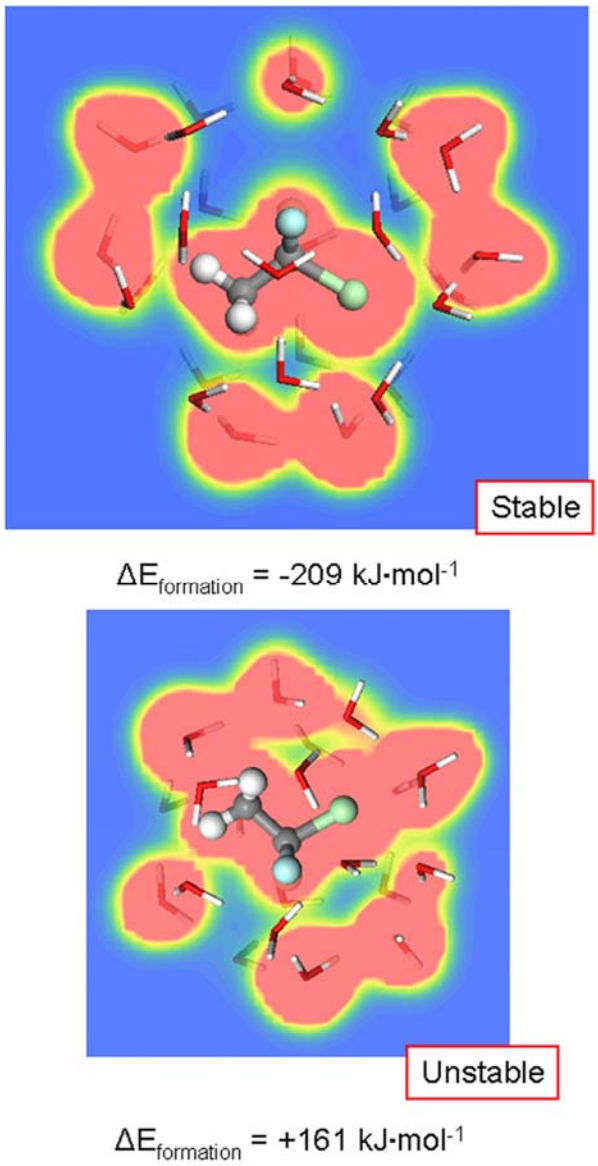

Figure 17. Optimized R141b-water clusters derived from DFT quantum calculations for the large water cavity (top) and the small water cavity (bottom) of R141b hydrate. The color map represents the electron density, and indicates the formation of strong interactions between coordinating water molecules and the R141b guest in the small cage.

Figure 17 provides a graphical comparison of the electron density derived from the calculations, and clearly shows significant overlap of the organic molecule with the water molecules of the small cavity leading to this destabilization. Electron density derived for the large cavity model shows the isolated R141b electron density distinct from that associated with the water molecules, which exhibit several pairs of prominent hydrogen bonds within the plane of the electron density map. The formation energies for the clathrate cluster with *gauche* and *anti* configurations of **2** are slightly less stable than that calculated for the clathrate with **1**. The *gauche* isomer clathrate is

more stable than the *anti* isomer even though the isolated *anti* isomer has a lower energy (4 $kJ \cdot mol^{-1}$) than the *gauche* isomer. This stabilization is primarily due to the ability of the *gauche* isomer to coordinate the chlorine atoms to the nearby water molecules rather than those across the cavity that would be limited by the *anti* configuration of chlorine atoms. Calculations for the optimized periodic hydrate models indicate the stability of the R141b hydrate relative to that for the *gauche* isomer by 147 $kJ \cdot mol^{-1} \cdot (\text{unit cell})^{-1}$. This energy difference is small compared to the potential energy difference observed ($kJ \cdot mol^{-1} \cdot (\text{unit cell})^{-1}$) in the classical simulations for the same two systems (see below). This comparison of simulation results emphasizes the limitation of DFT methods in accounting for intermolecular dispersion for systems such as hydrates involving guest-cavity interactions.[78-80] The empirically derived force field parameters used in the classical simulations provide a more accurate evaluation of these electron correlation effects.

The fully optimized periodic hydrate structures provide confirmation of the water oxygen positions observed by McMullan and Kvcik [70] for the structure II hydrate. We observe local perturbations of the oxygen position (~1.0 Å difference) for about 10% of the water molecules when associated with the organic guest, but overall there is very good agreement for the remaining water oxygen positions (0.22 ± 0.17 Å difference). Additionally, periodic DFT results support the optimized hydrogen bonding configuration as derived through the classical simulations. Finally, we compared the hydrate forming abilities of **1** and **2** by calculating the largest "molecular diameter" from the DFT electron density of each molecule. Following the method of Hout and Hehre, [81] a surface contour of 0.002 $e \cdot Å^3$ was used, which corresponds to van der Waals radii. The calculated molecular diameters were 6.8 Å (**1**) and 7.4 Å **(2**). Using the estimate of 6.6 Å as the "free diameter" inside a large cage of structure II hydrate,[82] it is apparent that isomer **2** is too large to fit inside the large cage of a structure II hydrate.

5.2.5 Classical Molecular Dynamics

All force field simulations discussed below were performed in the *NVT* ensemble at 265 K, with lattice parameters corresponding to the *NPT*-averaged values as discussed previously. We first investigated the effect of water mobility on guest-host interactions. Radial distribution functions (RDFs) between guest atoms (Cl, F, and H atoms) and water molecules (H_w and O_w atoms) are shown for **1** and **2** in Tables 3 and 4. For R141b (**1**), the Cl-H_w and F-H_w peak data are nearly identical, regardless of water mobility (Table 3). However, Table 4 shows a loss of structure when the isomer (**2**) hydrate is modeled with mobile water molecules. Further comparisons of hydrate structure between **1** and **2** were made based on simulations of immobile water molecules. Figure 18 shows the Cl–H_w and F–H_w RDFs. For **2**, the Cl–H_w and F–H_w peaks are shifted inward by 0.19 Å and 0.36 Å, respectively. The larger diameter of **2** (7.4 Å compared to 6.8 Å for R141b) results in smaller guest-water distances, as quantified in Table 5 by comparing X-H_w (X = Cl, F) coordination numbers at a distance of 3.0 Å (immobile water molecules). This distance falls within the range of hydrogen bond lengths for both Cl-H_w pairs (2.86 Å - 3.21 Å) and F-H_w pairs (2.62 Å - 3.01 Å).[83] The larger coordination numbers for **2** again indicate a closer interaction with the water cage due to size constraints. When the isomer hydrate system was simulated with mobile water molecules at 265 K, the hydrate structure dissociated into aqueous and organic phases. Only at much lower temperatures is the isomer hydrate stable. As

discussed previously, our calculated molecular diameters for **1** (6.8 Å) and **2** (7.4 Å) suggest that size effects should be considered when predicting the ability of these isomers to form hydrates. Finally, we note that the average potential energy of the R141b hydrate simulation is approximately 7100 $kJ \cdot mol^{-1}$ lower than that of the isomer. These results highlight the ability of molecular simulations to examine trends in hydrate stability.

Table 3. Radial Distribution Function (RDF) results for R141b hydrate (1).

	Immobile Water			Mobile Water		
RDF pair[a]	Peak Max / Å	Peak Min / Å	CN[b]	Peak Max / Å	Peak Min / Å	CN
Cl-H_w	3.15	3.91	0.71	3.19	3.91	0.70
F- H_w	3.19	3.91	0.34	3.13	3.79	0.29
H-H_w	2.85	3.49		2.93	3.49	
H-O_w	3.04	4.05		3.09	3.99	

[a]Hw and Ow refer to water H and O atoms, respectively.
[b]Coordination number calculated at an interatomic distance of 3.0 Å.

Table 4. RDF results for 1,2-dichloro-1-fluoroethane hydrate (2).

	Immobile Water			Mobile Water		
RDF pair[a]	Peak Max / Å	Peak Min / Å	CN[b]	Peak Max / Å	Peak Min / Å	CN
Cl-H_w	2.96	3.75	0.59	3.23	3.93	0.70
F- H_w	2.83	3.57	0.25	3.07	3.71	0.27
H-H_w	3.27			3.19	3.29	
H-O_w	3.53	4.91		3.15	4.41	

[a]Hw and Ow refer to water H and O atoms, respectively.
[b]Coordination number calculated at an interatomic distance of 3.0 Å.

Table 5. Halogen-water Coordination Numbers for hydrates of 1 and 2 measured at 3.0 Å.

RDF pair[a]	R141b (**1**)	Isomer (**2**)
Cl-H_w	0.12	0.17
F- H_w	0.06	0.11

[a]Hw and Ow refer to water H and O atoms, respectively.

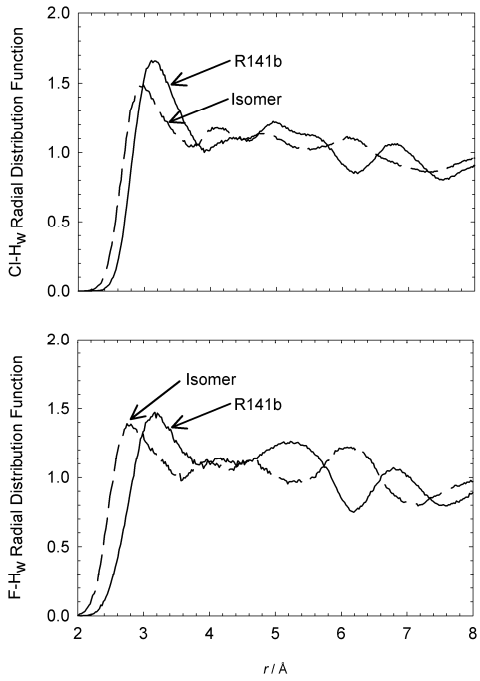

Figure 18. Cl-H_w (upper) and F-H_w (lower) RDFs for R141b hydrate (1) and the isomer hydrate (2).

We also attempted to quantify the rotational motion of **1** and **2** within the water cages. First, we examined the time-dependence of the mean-square-displacement (MSD) [74] for both Cl and F atoms in an attempt to see a difference in atomic diffusivity between the isomers. For **1** and **2**, the MSD values reached plateaus after 5.0 ps (data not shown), which is characteristic of solids and not gases or liquids. The plateau value for Cl and F atoms in R141b hydrate (6.3 $Å^2$) and the isomer (7.4 $Å^2$) mirrors the difference in van der Waals diameter of the two molecules, which reinforces the concept that the isomer requires a larger volume than is available in a structure II hydrate (Figure 17). Second, the (*x*, *y*, *z*) trajectories of F atoms in R141b hydrate were plotted, with an example shown in Figure 19. During the shorter simulation of 40 ps, only a portion of the free volume within the cage was sampled by the F atom (Figure 19, top). However, a trajectory from a longer 1000-ps simulation shows that the F atom mapped out the entire free volume of the cage (Figure 19, bottom). The same behavior was seen by both isomers, so we conclude that the difference in hydrate stability between **1** and **2** is caused mainly by intermolecular (hydrogen bonding, van der Waals) interactions due to size effects. The confined space within the large cage did not appear to hinder the rotational motion of either isomer.

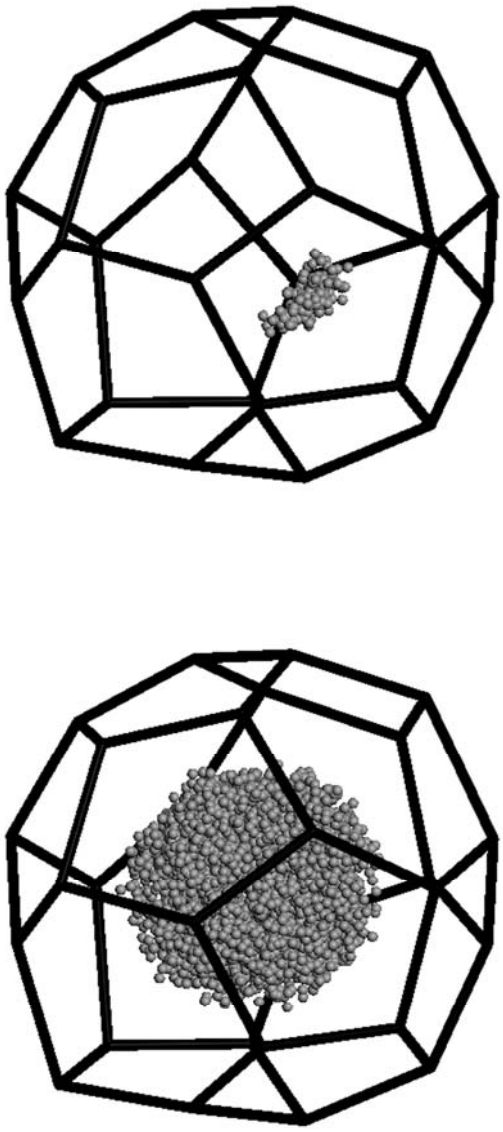

Figure 19. **Trajectories (gray spheres) of a fluorine atom in a large cage R141b hydrate during a 40-ps NVT simulation (top) and a 1000-ps simulation (bottom) of R141b hydrate. The spheres represent the location of the F atom every 0.25 ps during the simulations. The black lines represent the immobile water cage, with water oxygen atoms at each vertex.**

5.3 Vibrational Analysis of R141b Hydrate

A comparison of the calculated DFT vibrational spectra for the optimized cluster model of R141b and R141b clathrate is provided in Figure 20. Although a scaling factor is often used to correct quantum-based frequencies for comparison to experimental spectra, [78] no such corrections are made in this study; emphasis is placed on the relative changes in the vibrational energy and peak position. Calculations for the cluster model of R141b generated 18 active modes ($3N$-6 where N = number of atoms) once the molecular translations and rotations were removed. In the mid-infrared region, the R141b spectrum is dominated by C-F and C-Cl stretch modes. Bending modes involving the halogen and carbon atoms occur at lower frequencies (less than 600 cm^{-1}), while those involving C-H bends are observed between 1100 cm^{-1} and 1500 cm^{-1}. Stretch modes for C-H occur at the highest frequencies (~2700 cm^{-1}) and are characterized by relatively small intensities. These spectral features are generally consistent with experimental values as provided by Nakanishi and Solomon.[84]

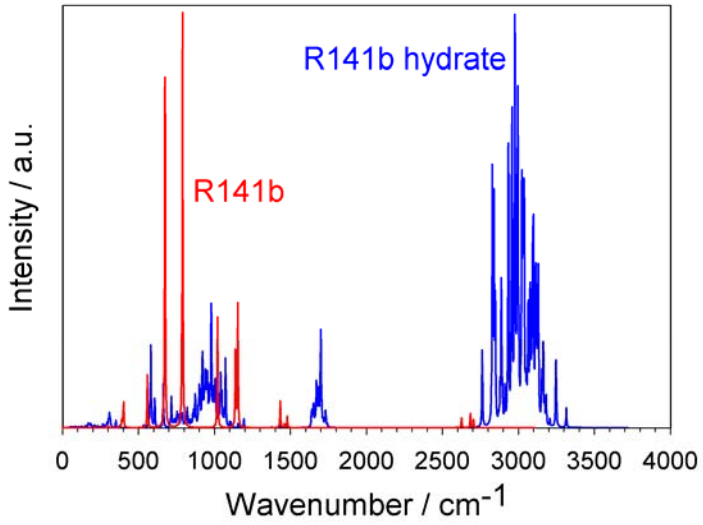

Figure 20. Calculated DFT vibrational spectra obtained from mode analysis of optimized cluster models from DFT for R141b (red) and R141b hydrate (blue).

The calculated spectrum for R141b hydrate is more complex due to the large number of combination modes associated with the large hydrogen bonding network of water molecules. The spectrum is characterized by a large group of high frequency O-H stretch modes (2700 cm^{-1} - 3300 cm^{-1}) associated with the water molecules. The associated H-O-H bend modes are observed at approximately 1700 cm^{-1}. The libration modes for the water molecules dominate much of the region from 300 cm^{-1} to 1200 cm^{-1}, while the relatively small intensities for the R141b molecule within the large cavity are observed at 605 cm^{-1} and 904 cm^{-1}, respectively for the C-Cl and C-F stretch modes. Considering the limitations of the DFT method, the calculated spectra are generally consistent with those observed by classical simulation (see below). Animation of the vibrational modes associated with the R141b molecule suggests the C-Cl stretch at 559 cm^{-1} is most sensitive to hydration and exhibits a shift to higher frequency.

The vibrational power spectrum of R141b hydrate obtained from the classical molecular dynamics simulations is shown in Figure 21. The overall spectrum is dominated by contributions from water molecules, but peaks due to R141b are visible after re-scaling their intensities. The water modes can be classified as follows: O–H stretch (3600 cm^{-1} – 3750 cm^{-1}), H–O–H bend (1500 cm^{-1} – 1700 cm^{-1}), and librations (400 cm^{-1} – 1000 cm^{-1}). Similarly, for R141b, the modes are: C–H stretch (2850 cm^{-1} – 3050 cm^{-1}), C–F stretch and CH_3 bend (1400 cm^{-1} – 1550 cm^{-1}), C–C stretch (1200 cm^{-1} – 1300 cm^{-1}), C–Cl stretch (900 cm^{-1} – 1000 cm^{-1}), and CCl_2F bend (630 cm^{-1}). The spectrum due to water molecules in R141b hydrate is very similar to that of hexagonal ice (Figure 22). However, for both the high- and low-frequency modes, the ice spectrum shows a more detailed structure. The water peaks are in relatively good agreement with the Raman peaks of hexagonal ice at –4 °C (3150 cm^{-1} – 3375 cm^{-1}, 1640 cm^{-1}, and 600 cm^{-1} – 870 cm^{-1}).[85] The increased rotational motion of water molecules in the hydrate phase compared to hexagonal ice may explain the difference in fine structure between 3600 cm^{-1} and 3750 cm^{-1}.

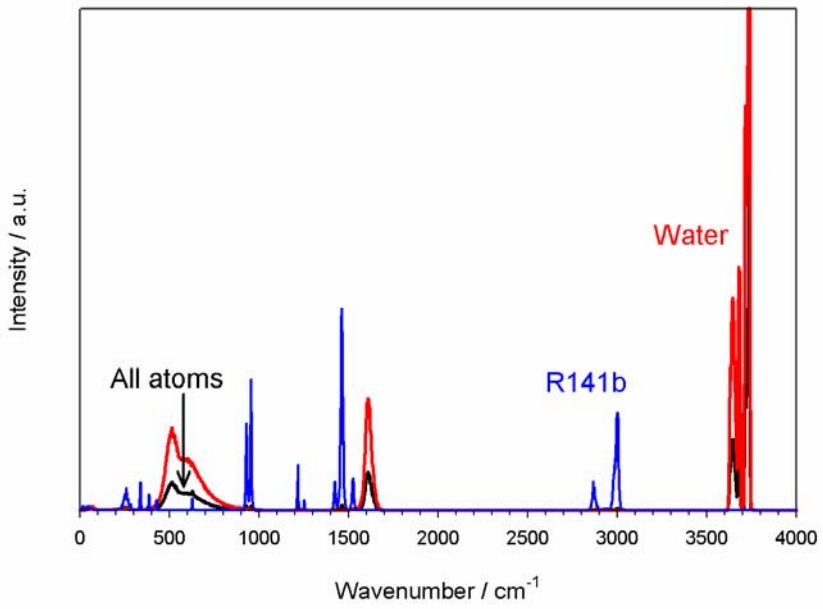

Figure 21. Simulated power spectrum of R141b hydrate (black line), showing contributions from water atoms (red line) and R141b atoms (blue line). Intensities of the R14b peaks were scaled to enhance visibility.

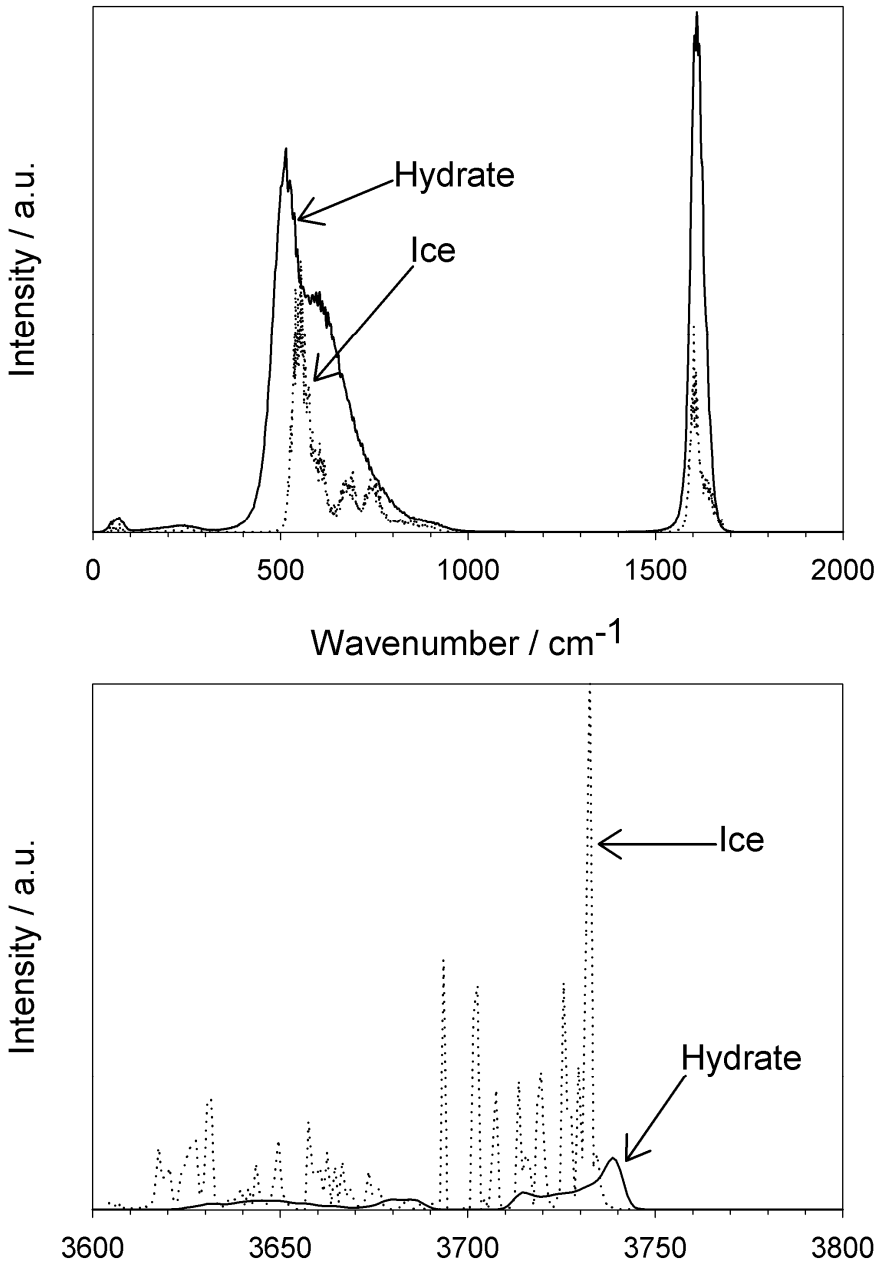

Figure 22. **Comparison of power spectra (H atoms only) of R141b hydrate (solid line) with hexagonal ice (dotted line). The intensities at lower frequencies (top) have been amplified for ease of viewing.**

A comparison of the R141b hydrate power spectrum with that of pure R141b is shown in Figure 23. For all bending and stretching modes that involve C–Cl or C–F bonds, hydrate peaks were shifted by 5 cm^{-1} to 10 cm^{-1} higher than those in pure R141b. Modes involving C–H bonds occur at identical frequencies in the two phases. No peak shifts were seen in the librational modes (< 500 cm^{-1}), which indicate that the nonbonding environment experienced by R141b in the two phases is similar. Despite the presence of hydrogen bonds between halogen atoms and water molecules (Table 2), the overall hydrophobic effect of R141b surrounded by water molecules is a strengthening of intramolecular interactions (blue shift in bonded modes) with no change in intermolecular interactions.

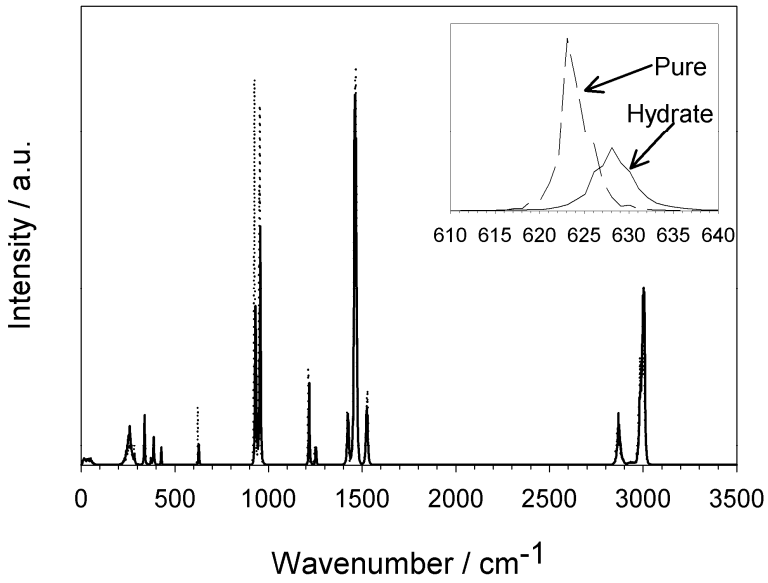

Figure 23. Simulated power spectrum of R141b in both the hydrate and (pure) gas phases. The inset shows the peak shift at 628 cm^{-1}.

5.4 Hydrate Synthesis and Characterization

The 0°C Raman spectra for R141b hydrate and pure liquid R141b are shown in Figure 24. Table 6 shows the peak fit data, and calculated peak shifts. The 586.03 cm^{-1} peak in the liquid reference spectrum is split in the hydrate, as shown in Figure 25. It was necessary to use two pseudo-Voigt peaks to obtain a satisfactory fit to this region of the hydrate spectrum, while the liquid reference spectrum was easily fitted with a single pseudo-Voigt. The most likely analog to the 586.03 cm^{-1} peak in the Raman spectrum occurs in the computational spectra at 559 cm^{-1} (DFT, Figure 20) and 628 cm^{-1} (MD simulation, Figure 23). This peak is comprised of a bending mode involving C, Cl and F atoms, and the hydrate peak is shifted approximately 7 cm^{-1} higher than the pure R141b peak in both computational calculations. As noted above, the confining effects of the water cage results in higher vibrational frequencies for bonded modes in the R141b spectrum.

The temperature-induced shift of the R141b liquid peak at 586 cm^{-1} is less than 0.3 cm^{-1} between –78°C and 0°C (data not shown). The splitting and relative shifts of the peaks in the hydrate sample at this Raman shift are larger than 0.3 cm^{-1} (Figure 26), and may indicate small changes in the R141b vibration frequencies due to interactions with the cage walls. There was difficulty obtaining a good fit to the hydrate peaks at 3002 cm^{-1} and 3017 cm^{-1} in the wavenumber regions corresponding to peaks at 3004.7 cm^{-1} and 3020.4 cm^{-1} in the reference spectrum. The fitting difficulties in this region were due to the large signal in the clathrate sample from peaks at 3159 cm^{-1} and 3343 cm^{-1}.

Table 6. Fitted peak positions in R141b hydrate, and liquid R141b reference, at 0°C.

R141b Hydrate		R141b Liquid Reference		
Raman Shift [cm^{-1}]	Error	Raman shift [cm^{-1}]	Error	Peak Shift [cm^{-1}]
255.75	0.06	255.99	0.05	-0.24
290.19	0.24	290.75	0.15	-0.56
374.81	0.04	374.67	0.04	0.14
392.04	0.09	392.75	0.10	-0.71
428.07	0.03	428.07	0.04	0.00
585.17	0.05	586.03	0.01	-0.86
593.44	0.10	586.03	0.01	7.42
740.00	0.09	740.23	0.10	-0.23
915.86	0.17	915.67	0.18	0.18
1082.96	0.30	1083.16	0.27	-0.20
1109.10	0.14	1108.26	0.11	0.84
1151.43	0.47	1150.94	0.43	0.49
1380.13	0.33	1380.21	0.39	-0.08
1433.48	0.10	1434.24	0.12	-0.76
2748.12	0.09	2747.66	0.10	0.46
2858.06	0.14	2857.73	0.17	0.33
2944.42	0.02	2943.24	0.02	1.18
3002.48	0.64	3004.68	0.29	-2.20
3017.39	1.05	3020.37	0.44	-2.98
3159.40	0.23	--		
3343.36	0.69	--		

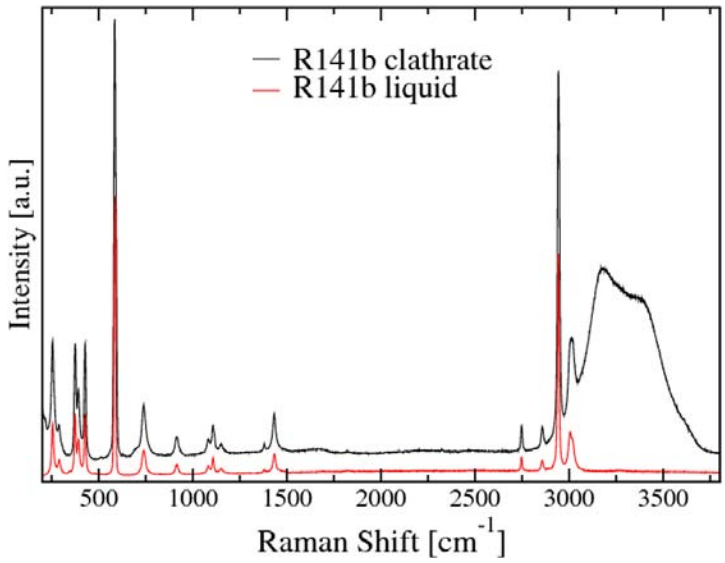

Figure 24. **Raman spectra of R141b hydrate (black line) and liquid sample (red line) at 0°C, using a 532 nm laser line. Peak shifts between the clathrate and liquid sample are below 1 cm^{-1}, except in the region near 586 cm^{-1}, and above 2900 cm^{-1}, as discussed in the text.**

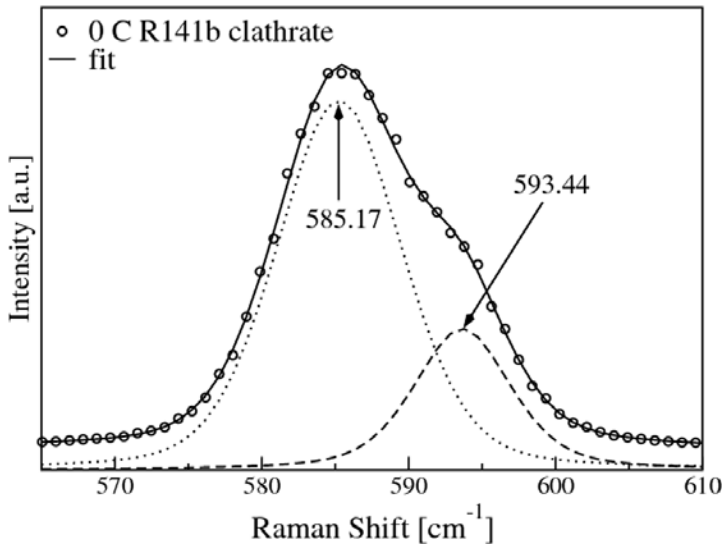

Figure 25. **Peak splitting at 586 cm^{-1} in the R141b hydrate sample at 0°C. Two pseudo-Voigt peaks (dashed line) were required for a satisfactory fit to the clathrate sample data. The liquid reference peak (dotted line) shows no splitting.**

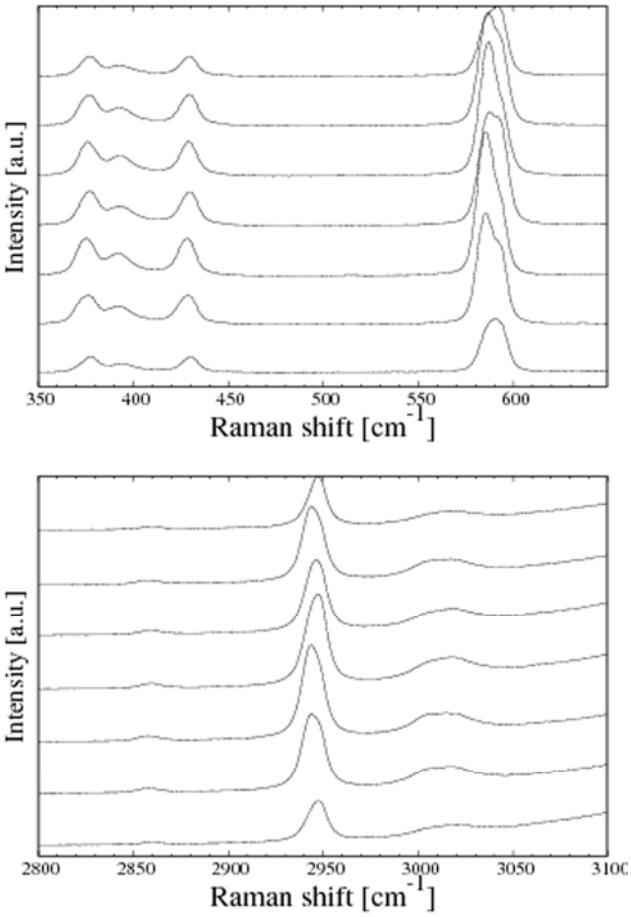

Figure 26. **Raman spectra of R141b hydrate as a function of temperature at low frequencies (top) and high frequencies (bottom). The scan temperatures from bottom to top are -4 °C, -2 °C, 0 °C, 1 °C, 2 °C, 3 °C, 4 °C, respectively. The peak at about 586 cm^{-1} (top) exhibits splitting and intensity variation, indicating that the associated molecular vibration is influenced by interactions with the cage. Peaks at higher frequency (bottom) are also shown.**

5.5 Conclusion

Despite their potential for forming hydrogen bonds with water cages, halogenated hydrocarbons appear to be good candidates for gas hydrate formers. The thermodynamic properties of these molecules and their hydrate formation make them good candidates for water desalination processes. We have carried out a combined computational and experimental study of hydrates formed from a prototype HCFC, R141b (**1**). Computational efforts were used to explain why **1** can form structure II hydrates at STP, but its **2** cannot. Significant orbital overlap exists between **2** and water molecules in either small or large cages of structure II hydrates. Our orbital overlap results were verified by comparing molecular diameters using a surface contour method to map the DFT electron density. We plan to extend our method of calculating molecular diameters to update the tables of host diameters obtained from geometric and van der Waals radii

considerations. It is important to note that the DFT calculations represent 0 K results and may be limited in extrapolation to real temperatures such as 265 K where the R141b hydrate is stable. Classical simulations (Figure 19) indicate that R141b molecules are in dynamical equilibrium with all water molecules in the large cavity of the hydrate and are not fixed at any local coordination. Additionally, the *anti* and *gauche* isomers of **2** are found to have a relatively small energy barrier between conformers and both can occur in the equilibrated systems.

X-ray diffraction results of R141b hydrate indicate a crystallography consistent with structure II unit cell. Constant-pressure simulations show that R141b hydrates are stable at ambient pressure up to 265 K, which is slightly lower but in good agreement with the experimental limit of 279 K. Peaks in the Raman spectra were assigned based on calculated vibrational spectra from DFT simulations. Of particular note is a shift in R141b vibrational modes between the liquid and hydrate phases. No shift was seen in the low-wavenumber librational modes, so the local (nonbonding) environment around R141b molecules in both phases is similar.

This page has been intentionally left blank

6. Spectroscopy of R141b Hydrates

Clathrate hydrate samples were characterized by x-ray diffraction and Raman spectroscopy. Samples for x-ray diffraction were removed from a -22°C freezer and ground under liquid nitrogen into a fine powder. The samples were placed on a cold plate held at approximately 0°C and covered with mylar to prevent condensation of water vapor on the sample. Diffraction spectra were collected on a Scintag XDS-2000, in Bragg-Brentano geometry. Figure 27 shows x-ray diffraction spectra from R141b clathrate. The data are indexed by a combination of structure II peaks and hexagonal ice (I-hex) peaks, [86] indicating some residual water was frozen in part of the process or during sample preparation. The structure II peaks match expected reference peaks at values of 2-theta below 30 degrees, with a small systematic mismatch at higher diffraction angles. This is likely due to a shift of the sample surface height on the diffractometer stage during the sample run. All the diffracted peaks fall to the left of the expected lines, indicating a change in the sample height due to partial melting of the clathrate during data collection.

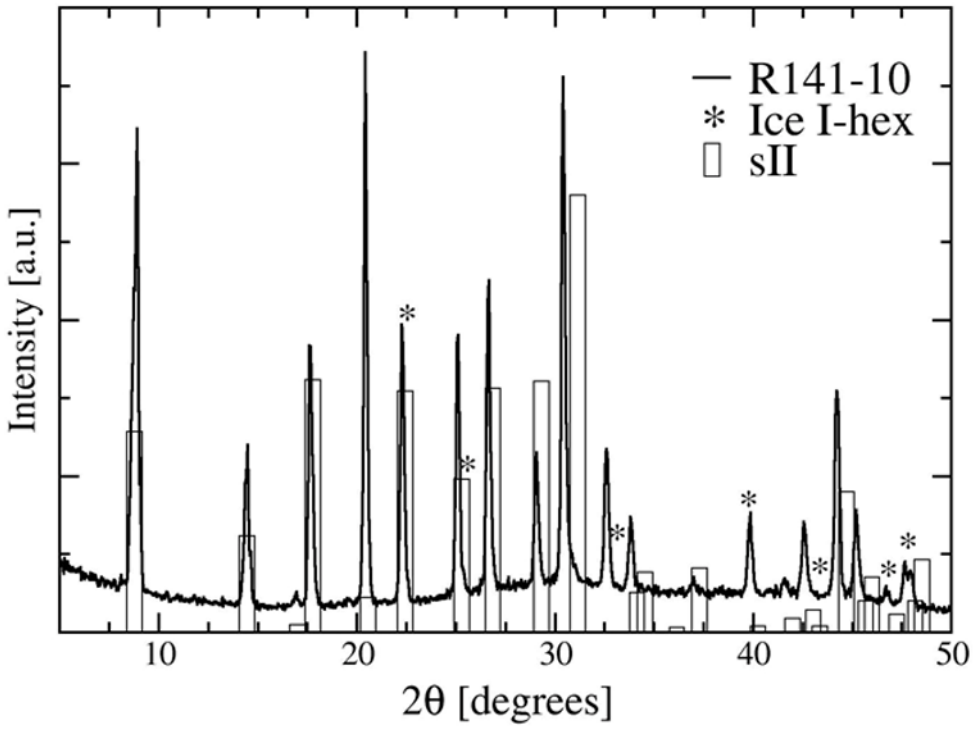

Figure 27. X-ray diffraction spectrum of R141b clathrate hydrate (black) compared to structure II clathrate hydrate peaks (green) and hexagonal form of water ice (red).

No Raman spectra of R141b hydrates appear to be available in the literature. Raman spectra were collected on a Princeton Instruments 0.75m SpectraPro 2750 triple grating spectrograph, using the 632 nm line from a He-Ne laser. Collection time for all samples was 10s, with a power at the sample of approximately 10mW. Clathrate samples were kept at approximately -6°C on a cold stage during the collection time. A liquid R141b reference spectrum was taken at room temperature. The Raman spectra are shown in Figure 28. The scattered signal from the clathrate samples is rather low in intensity. The most visible Raman peak in the clathrate samples occurs at 588 cm^{-1}, and shows a small shift to higher wavenumber with respect to the R141b liquid reference peak at 586.2 cm^{-1}. Lowering the temperature of the R141b liquid to -78°C (dry ice) does not result in a shift of the 586.2 cm^{-1} peak. The significance of the observed shift is not entirely clear based on these preliminary data. The 2-wavenumber shift of the peak in the clathrate samples may indicate small changes in the R141b vibration frequencies due to interactions with the cage walls. Alternatively, the shift may be the result of a lack of R141b liquid-liquid interactions.

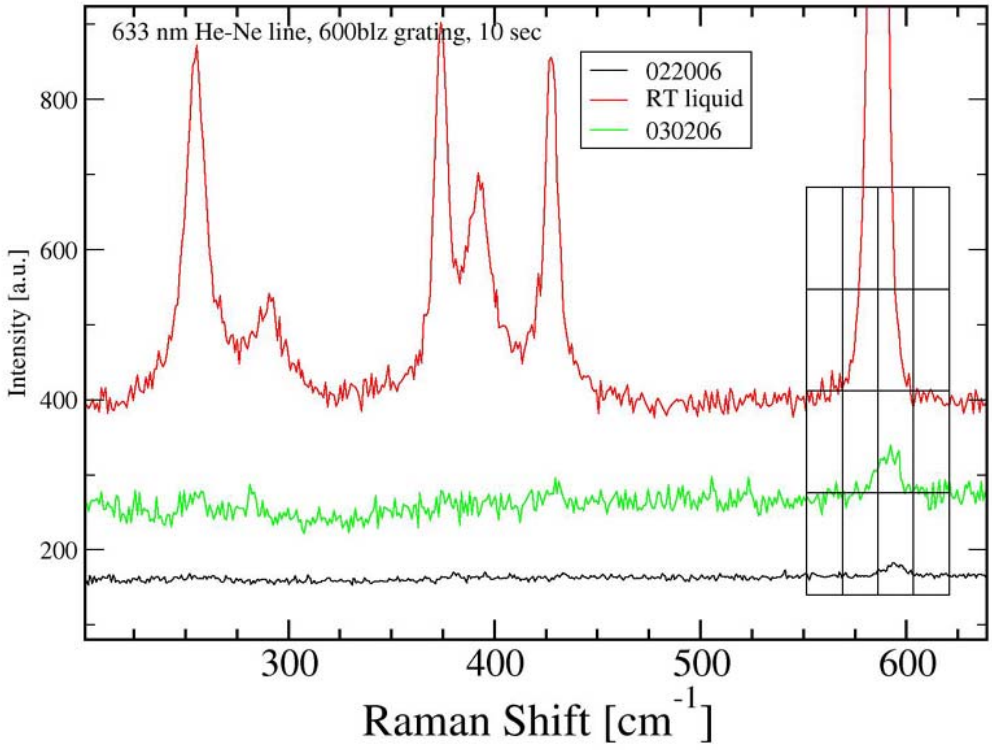

Figure 28. Raman spectrum of R141b clathrate hydrate (green and black) compared to liquid phase R141b (red).

7. HFC-32 Hydrate Formation

HCFC (hydrochlorofluorocarbon) compounds, such as R141b, are restricted by recent environmental regulations because of their ozone-depleting potential and are no longer practical candidates for a hydrate desalination process. Although this is unfortunate because of the ease of use of R141b as a liquid hydrate guest, several excellent alternatives that are environmentally acceptable were identified among HFC (hydrofluorocarbon) compounds. Among these are HFC-32 (difluoromethane) and R152a (difluoroethane), which form stable hydrates at relatively high temperature and moderate pressure. Akiya determined the equilibrium behavior of the difluoromethane-water-hydrate system and reported a critical stability temperature of 21°C and a critical stability pressure of 1.5 mPa, equivalent to 210 psi.[87] At 15°C, the equilibrium pressure of HFC-32 hydrate is about 100 psi which is quite moderate for process vessel construction. The structure of the HFC-32 hydrate is sI and the corresponding hydration number is 5.7, if all of the small cages of the sI structure are occupied by HFC-32 molecules.

A matrix of hydrate formation experiments emphasizing HFC-32 and R152a was performed in the third year of the LDRD. A brief discussion of the results regarding hydrate formation experiments with HFC-32 is presented here to illustrate the significant advantages and promising outlook for applying this type of gaseous guest molecules to hydrate desalination. A full discussion of the experimental results concerning hydrate formation with the gaseous guest species HFC-32, R152a and ethylene are reported in another document.[88]

Experimental trials demonstrated that HFC-32 clathrate hydrates formed spontaneously in deionized water and saline solutions without the assistance of secondary nucleation. In a few preliminary experiments conducted below 8°C (the stability temperature of R141b hydrates), a small amount of R141b hydrate solids were used to secondarily nucleate HFC-32 hydrate growth. The use of the seed material was discontinued given subsequent observations of primary (homogeneous) nucleation and, of course, was not feasible with experiments conducted at temperatures above 8°C. The pressure-temperature-time profile of a typical hydrate formation experiment is shown in Figure 29. The left ordinate scale gives the HFC-32 pressure (psi units) and the right ordinate scale gives the temperatures (degrees Celsius) of the two thermocouples placed in the portion of the cell initially filled with saline solution. The plot shows that pressure continuously decreased with time as HFC-32 was absorbed from the gas phase by hydrate formation. Some liquid HFC-32 was formed at the outset of the experiment because the initial pressure of the HFC-32 reservoir exceeded the vapor pressure of HFC-32 at the experimental temperature. The temperature profiles demonstrate the expected corollary behavior, that the heat of hydrate formation is transferred to the hydrate-saline slurry as sensible heat. The heat of hydrate fusion is released much more rapidly that contents of the cell can be cooled by heat transfer to the coolant circulating in the cell jacket. Local formation of hydrates at or near the thermocouples, apparently due to agglomeration and growth of hydrates on the sheaths, are likely to be the cause for the extremely rapid increases in temperatures indicated in the plot at 400 to 500 seconds of elapsed time. The final pressure the experiment approached the equilibrium pressure of approximately 100 psi at 10°C.

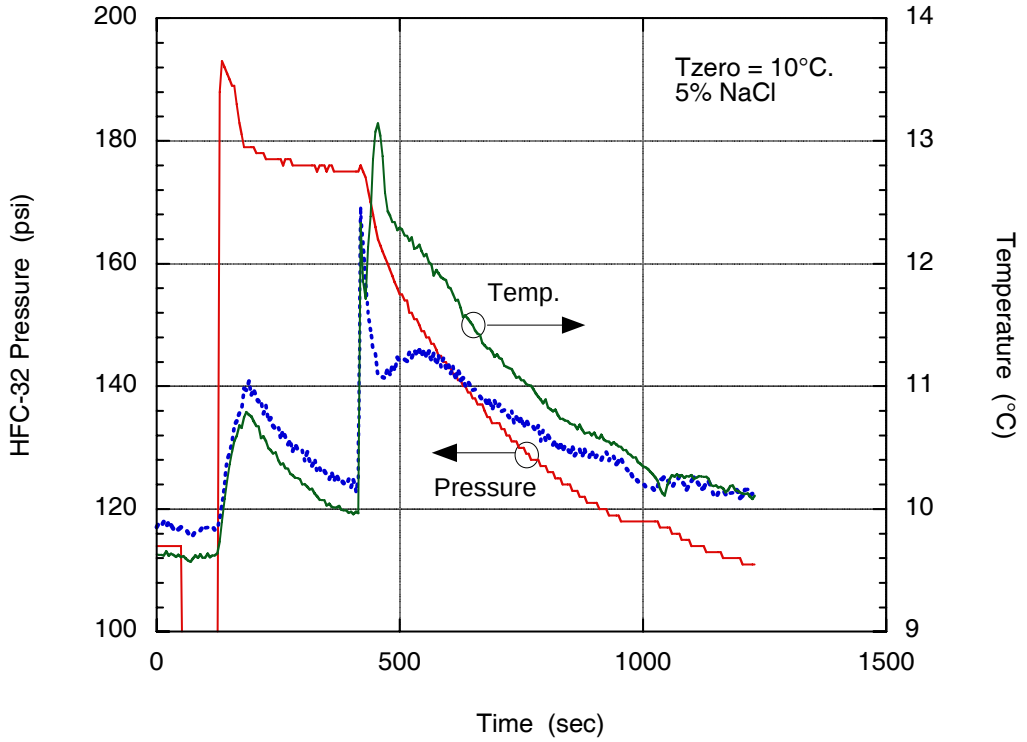

Figure 29. HFC-32 clathrate hydrate formation in 5% saline solution at an initial temperature of 10°C. The pressure is given by the left ordinate and the cell temperatures by the right.

A photo of the HFC-32 hydrates formed during an experiment is shown in Figure 30. The hydrates, visible as white, roughly spherical particles an mm or two in diameter, appear to be more dense than saline and generally settled to the bottom. These observations were made at atmospheric pressure, so the HFC-32 hydrate was not stable and the particles were gradually decomposing and off-gassing.

The rate of hydrate formation by a gaseous guest molecule can be calculated from the rate of pressure decrease, assuming full occupancy of the sI structure by HFC-32 molecules. For the experiment depicted in Fig. 29, the average rate of water uptake was 0.56 x 10^{-3} mol/sec. This rate is comparable to that reported in a preceding section for R141b hydrate formation. An impeller shape specifically designed for optimizing gas dispersion in liquids was not available in a diameter small enough to fit into the test cell used for these experiments. The impeller type and arrangement for mixing the gas and liquid phases in these experiments therefore yielded hydrate formation rates that very likely represent a lower limit on what could reasonably be achieved in a properly agitated large-scale production reactor. In addition, a continuous type of hydrate reactor would be operated at constant HFC-32 pressure, which would produce in faster rates than determined by averaging over a large pressure drop in these experiments.

Figure 30. HFC-32 hydrates, which are visible as white particles, were formed in a 3.5 wt.% NaCl solution at 10°C in a stirred batch reactor. The elapsed time of this experiment was approximately 1200 seconds although most of the hydrates formed in a shorter period.

The hydrate formation rates determined here are meaningful primarily as comparisons among the various conditions of temperature and salinity at which the rates were determined. However, the present data enable rough calculations of the size of the hydrate forming reactor and thus may be considered as a lower bound on rates that could be achieved. Regardless, an estimate of the rate of production of hydrates can be made from these data. For example, assume a hydrate reactor operates at 10°C and 5 wt.% NaCl (the inlet seawater concentration, 3.5 wt.% NaCl, must significantly increase within the reactor in a viable process scheme), corresponding to a water uptake rate of 5.6×10^{-4} mol/sec according to the calculation above. The volume of the experimental reactor was approximately 400 mL. The per liter production rate is then 1.4×10^{-3} mol/sec/L. Given a desalination reactor volume of 1000 liters, a relatively modest size, the rate at which water is removed from the saline feed (for subsequent separation by decomposing the hydrate) is 1.4 mol/sec which corresponds to 0.95×10^{2} liter/hour.

The results of several experiments which demonstrated the extraction of water from brine after HFC-32 hydrate formation in a stirred batch reactor at various temperatures are collected in Table 7. Samples of hydrate materials were removed from several experiments conducted at various initial values of salinity and temperature. The reduction in the salinity of melted HFC-32 hydrates was typically about 50%. Collecting samples at atmospheric pressure was problematic

because the hydrates were actively decomposing and were contaminated by the residual brine to an extent that was not well controlled. Thus, these data represent lower limits on the separation and recovery of water that could be achieved in a large-scale system at process pressure. These separations results are discussed in greater detail elsewhere.[88]

Table 7. Separation of water from brine by HFC-32 hydrate formation in a stirred batch reactor at various temperatures

Temp. (start)	Pressure (start)	NaCl Conc. (start)	NaCl Conc. (final)	Hydrate samples NaCl conc.
°C	psi	wt%	wt%	wt%
10	160	5.03		3.57
10	150	3.44		1.91
5	170	2.04		0.89, 1.23
10	150	2.04	3.21	n.a.

8. Hydrate Desalination Process Development

A simplified flowsheet of a hydrate desalination process is shown in Figure 31 which indicates the primary steps required to produce potable water from seawater; hydrate formation, separation of hydrates and brine, dissociation of hydrates to water and guest molecule. After the hydrates have been formed and separated, the heat exchange fluid/hydrate mixture will be pumped as a slurry to a separate chamber that will be at suitable temperature and pressure to disassociate the hydrates. The heat energy that is released during hydrate formation is conserved in the heat exchange fluid and is the same as the heat of hydrate disassociation. This can result in a very energy efficient desalination process if a large fraction of this energy can be recuperated. After dissociation, the hydrate forming species will dissolve into the heat exchange fluid and be recycled, and the water will separate from the heat exchange fluid. The cooled water stream may also be used in several applications that can increase the overall efficiency of the process.

The batch reactor was a useful tool for quantitative studies of hydrate formation using a variety of guest molecules and material phase combinations and for proof-of-concept work regarding the applicability of the novel heat transfer fluid method. The experimental results presented in this report concerning rates of hydrate formation indicate that kinetics will not be a constraint upon designing an efficient, cost-effective high capacity system. These results for R141b are reinforced by data for hydrate-forming agents that are not HCFC's, which are documented in a separate report.[88] A production-scale system will undoubtedly use a continuous flow stirred reactor design, based on higher throughput and process economic considerations. Hydrate formation kinetics for a continuous system will at least equal that determined in a batch system because of more uniform mixing and process conditions in the former.

Other factors that significantly affect the viability of a clathrate hydrate desalination process are separation of hydrate and brine and process economics related to cooling requirements. The small batch reactor used for hydrate formation studies was not an effective test bed for evaluating separations. However, the simple sampling methods possible with this configuration demonstrated the utility of the heat transfer fluid method. R141b hydrates tended to form relatively low-density, aggregated solid material that accumulated at the surface of the saline solution. In contrast, when used with a heat exchange fluid such as Fluorinert, a dispersion of hydrate-covered droplets was produced that were much more dense than water and settled to the bottom of the reactor. The basic concept of using a heat exchange fluid was found to potentially useful, although further development in a system resembling that which would be applied to a commercial process is needed using appropriate physical separation methods. more effective separation could be achieved at larger scales by widely used methods such as cold filtration or cold centrifugation.[89]

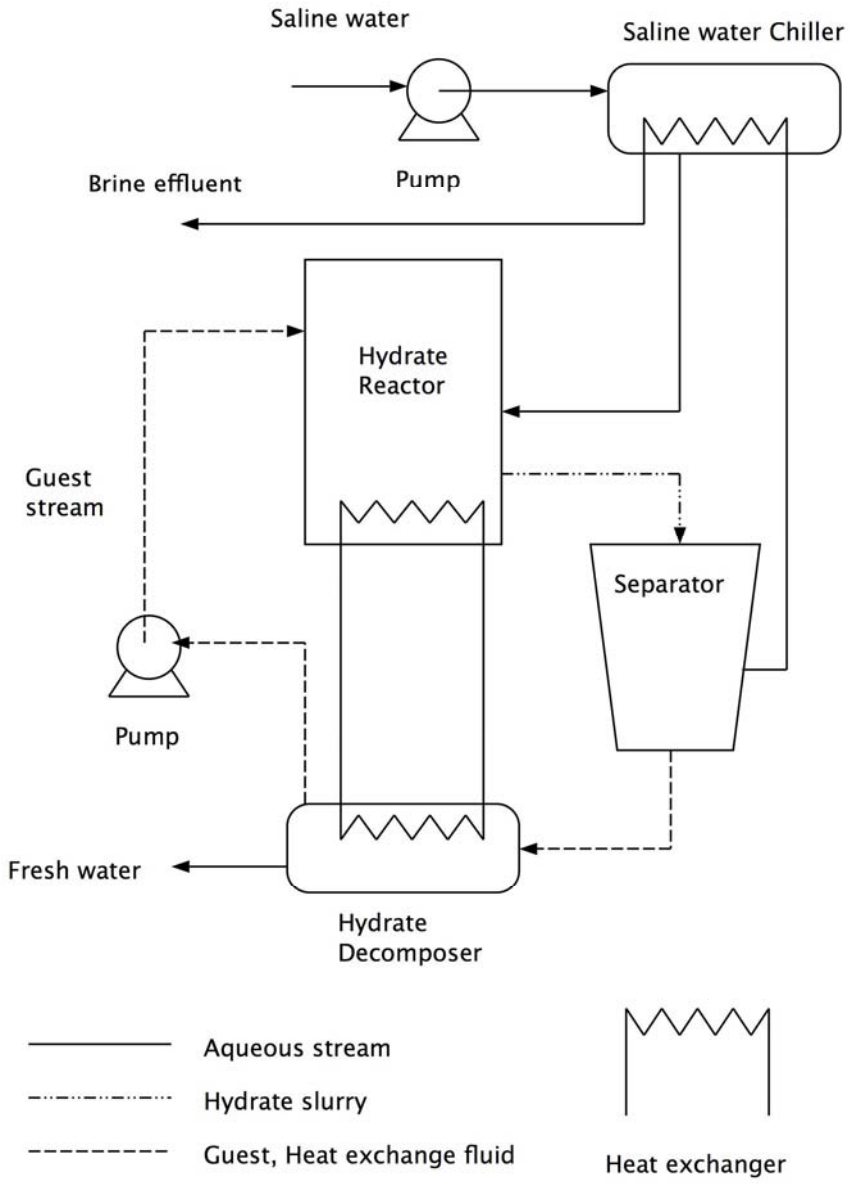

Figure 31. Simplified flowsheet of a continuous clathrate hydrate desalination process. Recuperative heat exchange is shown between the hydrate reactor and decomposer.

Process fluid cooling requirements will be necessary to a lesser or greater extent regardless of the relatively high temperatures at which a process using HFC-32 as the guest molecule could operate. It has been recognized recently that liquid natural gas (LNG) regasification produces very large amounts of chilled seawater at the outflow of the heat exchangers.[90] This chilled seawater is presently discharged back into the ocean due to the location of LNG tanker docking facilities. The current LNG facilities, as well as the anticipated growth in the use of LNG as an energy resource, offer the prospect of coupling a regasification system to a clathrate hydrate desalination process and thereby greatly reducing the cost of providing refrigeration to the latter. Alternatively, an especially interesting clathrate hydrate desalination process arrangement would be to use a gaseous guest molecule, such as HFC-32, as a refrigerant as well as the hydrate-forming agent. Process configurations employing such direct-contact secondary refrigeration have been demonstrated to provide for extremely efficient heat transfer to a hydrate-gas-liquid slurry reactor.[91]

This page has been intentionally left blank

9. Summary

The thrust of this LDRD project was to evaluate the properties of clathrate hydrates, both experimentally and by molecular dynamics simulations, as the basis of a desalination process. The development of clathrate hydrate technology as a scalable and reliable tool for desalination would result in significant improvement in the availability of water supplies for U.S. communities and industry. The method by which these impacts would manifest themselves can be clearly seen in a direct comparison with other technologies. Hydrate desalination will be more efficient in terms of water throughput and recovery when compared to reverse osmosis, while operating at much lower pressures, making for a more energy efficient process. There will also be a high degree of energy recuperation between hydrate formation and disassociation by utilizing an immiscible heat exchange liquid that provides for direct contact between water and hydrate guest molecules.

Two aspects of clathrate hydrate research have been pursued in this LDRD. Extensive experimental investigations were conducted to evaluate the rate of hydrate formation for a variety of guest molecules and the effect of inert heat exchange fluids on the formation rates and the separation of hydrates from brine. Molecular dynamics simulations have differentiated the stability behavior of guest molecules and their isomers that do not form stable hydrates, as well as predicting spectroscopic features of hydrate structures that were validated by Raman spectroscopy measurements.

The extensive experimental studies conducted in this LDRD demonstrate that the concept of using a heat exchange fluid is basically sound. The experiments also generated rate of formation data that are used for scale-up calculations for several hydrate formers. Hydrate formation experiments were conducted with the guest molecule R141b (a liquid, $C_2FCl_2H_3$) and the heat exchange fluid Fluorinert. Additional clathrate hydrate formation experiments were performed using several other hydrate guest molecules, including the gaseous species, HFC-32 (difluoromethane), R152a (difluoroethane) and ethylene. Cooperative hydrate formation whereby cyclopentane facilitates the formation of HFC-32 hydrate was also investigated.

The hydrate formation kinetics data produced by a matrix of approximately 60 experiments were analyzed to determine the rate equation describing R141b hydrate formation. The rate of R141b hydrate formation in deionized water and sodium chloride solutions containing 2%-7% (wt.) was measured at temperatures of 1°C to 6°C. Hydrates were formed in a stirred batch reactor in which these immiscible liquids were agitated to produce a complete dispersion and hydrate growth was initiated by secondary nucleation. The rates were determined from the temperature rise corresponding to the enthalpy of hydrate formation in this quasi-adiabatic closed system. The rate of R141b hydrates formation data were well correlated solely by the degree of supercooling of the saline solution according to an exponential equation. The rate data for pure R141b served as a baseline both for scale-up calculations for a production size system and to evaluate the effect of a heat exchange fluid. For example, assume an R141b hydrate reactor operated at 3°C and 5 wt.% NaCl (the inlet seawater concentration, 3.5 wt.% NaCl, must

significantly increase within the reactor in a workable process scheme), which corresponds to a water uptake rate of 5.3×10^{-4} mol/sec. Given a desalination reactor volume of 1000 liters, a quite modest size, the rate at which water is removed from the saline feed (for subsequent separation by decomposing the hydrate) is 2.65 mol/sec or 1.7×10^{2} liter/hour.

The effect of a heat exchange fluid on R141b hydrate formation was determined by a matrix of experiments in which R141b was dissolved in Fluorinert. R141b and Fluorinert are completely miscible liquids having low vapor pressure and the mixtures are immiscible with water, similar to pure R141b. In this matrix, saline concentration varied from 0-6 wt.% NaCl, temperatures were 1°C to 6°C and hydrate growth was initiated by secondary nucleation as before. The rate of hydrate formation was generally reduced by an amount corresponding to the mol fraction of R41b in the organic mixture, which was typically near 0.3. The rate data are well correlated by the same exponential functional dependence on the degree of supercooling of the saline solution. However, the rates also depended explicitly on the saline concentration. This latter effect may be due to the dispersion characteristics of the R141b-heat exchange fluid mixture in saline. Regardless, the results demonstrated that hydrate rates were well within a range that implies realistic scale-up to a production system.

The small batch reactor used for hydrate formation studies was not an optimal test bed for evaluating separations, and more effective separation could be achieved at larger scales by widely used methods, such as cold filtration or cold centrifugation. However, simple sampling methods demonstrated the utility of the heat transfer fluid method. R141b hydrates tended to form relatively light material that accumulated at the surface of the saline solution. In contrast, R141b-Fluorinert produced a fine dispersion of hydrate-covered droplets that were much more dense than water and settled to the bottom of the reactor. The basic concept of using a heat exchange fluid was found to be potentially useful, although further development in a system resembling that which would be applied to a commercial process is needed, using appropriate physical separation methods.

HCFC compounds, such as R141b, are restricted by current environmental regulations and are no longer practical candidates for a hydrate desalination process, despite their ease of use. Several excellent alternatives were identified among HFC compounds that form stable hydrates at high temperatures and moderate pressure. Among these compounds are HFC-32 (difluoromethane) and R152a (difluoroethane). HFC-32 hydrate formation data were acquired by a matrix of approximately 10 experiments in deionized water and sodium chloride solutions containing 2%-5% (wt.) at temperatures of 5°C to 15°C. Hydrates were formed in a stirred batch reactor in which hydrate growth was initiated by homogeneous nucleation. The rates were determined from the pressure drop as HFC-32 was consumed by hydrate formation. The rate of hydrate formation of HFC-32 was somewhat less than R141b because the former was contacted with saline solution in the gaseous state compared to the liquid state for the latter. However, a rate of HFC-32 hydrates formation approximately 30% that of R141b was achieved in a batch reactor at 10°C and 5 wt.% NaCl. Given a desalination reactor volume of 1000 liters, the rate at which water is removed from the saline feed (for subsequent separation by decomposing the hydrate) is 2.8 mol/sec which corresponds to 1.9×10^{2} liter/hour.

We completed a combined computational and spectroscopic study of structure II hydrates consisting of 1,1-dichloro-1-fluoroethane (R141b) or its isomer, 1,2- dichloro-1-fluoroethane. R141b forms a structure II hydrate phase at mild conditions (0 °C, 0 atm), occupying only the large cages. We studied the structure and dynamics of guest R141b molecules within water cages, obtained from *ab initio* calculations, molecular dynamics (MD) simulations, and Raman spectroscopy. Such information will be needed to understand and control the nucleation and growth of these hydrates for industrial applications. Density functional theory (DFT) calculations were used to provide an energetic and molecular orbital description of R141b stability in both large and small cages in a structure II hydrate. Additionally, the hydrate of an isomer, 1,2-dichloro-1-fluoroethane, does not form at ambient conditions due to extensive overlap of electron density between guest and host. Results for the isomer hydrate were supported by classical molecular dynamics simulations and synthesis attempts. Molecular dynamics simulations show that R141b hydrate is stable at temperatures up to 265K, while the isomer hydrate is only stable up to 150K.

The Raman spectrum of R141b in both the pure and hydrate phases was also compared with vibrational analysis from both computational methods. The Raman frequency of a carbon-halogen stretch mode (585 cm^{-1}) undergoes a shift to higher frequency in the hydrate phase. Raman spectra also indicate that this peak undergoes splitting and intensity variation as the temperature is decreased from 4°C to –4°C. Corresponding peaks were identified from DFT normal mode analysis (559 cm^{-1}) and MD power spectra (630 cm^{-1}).

The deployment of large-scale clathrate hydrate desalination capacity may not be realized in the near term, although a process development project at the pilot plant scale based on CO_2 hydrate formation is being pursued by a commercial engineering company.[92] Regardless, the results described here represent advances in several aspects of the technology necessary to develop an economical means to produce municipal quantities of potable water from seawater or brackish water. These aspects include the following, (1) advances in defining the most promising systems design based on new types of hydrate guest molecules, (2) selection of optimal multi-phase reactors and separation arrangements, and, (3) applicability of an inert heat exchange fluid to moderate hydrate growth, control the morphology of the solid hydrate material formed, and facilitate separation of hydrate solids from concentrated brine.

This page has been intentionally left blank

References

1. City of Tampa Bay, FL; http://www.tampabaywater.com/watersupply/mpdesal.aspx (2006).
2. City of Huntington Beach, CA; http://www.ci.huntington-beach.ca.us/citydepartments/planning/major/poseidon.cfm (2007).
3. E. D. Sloan, Jr., Clathrate Hydrates of Natural Gases, Second Edition, Marcel Dekker, New York, 1997
4. C. A. Koh and E. D. Sloan, A. I. Ch. E. J., 53 (7), 1636 (2007)
5. W. G. Knox, M. Hess, G. E. Jones and H. B. Smith, Chem. Eng. Progr., 57, 66 (1961)
6. Koppers Co., "Potable Water from Sea Water by the Hydrate Process", Office of Saline Water, Research Develop. Progress Report No. 90, 1964.
7. A. J. Barduhn, H. E. Towlson and Y. C. Lee, A.I.Ch.E. J., 8, 176 (1962)
8. R. A. McCormack and G. A. Niblock, "Investigation of high freezing temperature, zero ozone, and zero global warming potential, clathrate formers for desalination", U.S. Dept. of the Interior, Bureau of Reclamation, Water Treatment Technology Program Report 59, June 2000.
9. R. A. McCormack and G. A. Niblock, "Build and operate clathrate desalination pilot plant", U.S. Dept. of the Interior, Bureau of Reclamation, Water Treatment Technology Program Report 31, May 1998.
10. R. A. McCormack and R. K. Andersen, "Clathrate desalination plant preliminary research study", U.S. Dept. of the Interior, Bureau of Reclamation, Water Treatment Technology Program Report 5, June 1995.
11. J. E. Miller, "Review of Water Resources and Desalination Technologies", SAND 2003-0800, Sandia National Laboratories, p. 34 (2003)
12. R. Semiat, Water International, 25, (10), 54 (2000).
13. R. Ohmura, M. Ogawa, K. Yasuoka and Y. H. Mori, J. Phys. Chem. B, 107, 5289 (2003)
14. Topac, Inc., http://www.topac.com/Salinity_brix.html, (2002)
15. A. H. P. Skelland and G. G. Ramsay, Indust. Engg. Chem. Res., 26, 77 (1987)
16. H. Yamamura and K. Takahashi, J. Chem. Eng. Japan, 32 (4), 395 (1999)
17. G. Irvin, S. Li, B. Simmons, V. John, G. McPherson M. Max and R. Pellenbarg, Annals N. Y. Acad. Sci., 912, 515 (2000)
18. B. A. Simmons, R. W. Bradshaw, D. E. Dedrick, E. H. Majzoub, D. W. Anderson, “Complex Admixtures of Clathrate Hydrates in a Water Desalination Method”, Patent Application No. 11/489306, July 17, 2006.
19. Y. Xie, K. Guo, D. Liang, S. Fan, Chem. Engg. Sci., 60, 777 (2005)
20. Y. H. Bi, T. W. Guo, T. G. Zhu, S. S. Fan, D. Q. Liang and L. Zhang, Applied Energy, 78 (1), 111 (2004)
21. I. Kobayashi, Y. Ito and Y. H. Mori, Chem. Engg. Sci., 56, 4331 (2001)
22. J. Li, D. Liang, K. Guo and R. Wang, J. Coll. Interface Sci., 283, 223 (2005)
23. R. Ohmura, T. Shigetomi and Y. H. Mori, J. Crystal Growth, 196 (1), 164 (1999)
24. D. Liang, K. Guo, R. Wang and S. Fan, Fluid Phase Equil., 187-188, 61 (2001)

25. D. H. Brouwer, E. B. Brouwer, G. MacLaurin, M. Lee, D. Parks and J. A. Ripmeester, Supramolecular Chem., 8, 361 (1997)
26. D. Liang, K. Guo, S. Fan and R. Wang, J. Engg. Thermophys., 23, 47 (2002)
27. J. B. Pangborn and A. J. Barduhn, Desalination, 8, 35 (1970)
28. D. Kashchiev and A. Firoozabadi, J. Crystal Growth, 241, 220 (2002).
29. M. Arjmandi, B. Tohidi, A. Danesh and A. C. Todd, Chem. Engg. Sci., 60, 1313 (2005)
30. P. Engelzos and P. R. Bishnoi, A.I.Ch.E.J., 34 (10), 1718 (1988)
31. J. Javanmardi and M. Moshfeghian, Fluid Phase Equil., 168, 135 (2000)
32. H. Kubota, K. Shimizu, Y. Tanaka and T. Makita, J. Chem. Engg. Japan, 17 (4), 423 (1984)
33. A. J. Barduhn, H. E. Towlson and Y. C. Lee, A.I.Ch.E. J., 8, 176 (1962)
34. E. D. Sloan Jr., *Clathrate Hydrates of Natural Gases*; Marcel Dekker, Inc.: New York, 1998.
35. B. A. Buffett, *Ann. Rev. Earth Planet. Sci.*, 28, 477 (2000).
36. W. G. Knox, M. Hess, G. E. Jones and H. B. Smith, Chem. Eng. Progr., 57, 66 (1961)
37. Barduhn, A. J.; Towlson, H. E.; Hu, Y. C. *AIChE J.* **1962**, *8*, 176.
38. R. A. McCormack and G. A. Niblock, "Investigation of high freezing temperature, zero ozone, and zero global warming potential, clathrate formers for desalination", U.S. Dept. of the Interior, Bureau of Reclamation, Water Treatment Technology Program Report 59, June 2000.
39. D. H. Brouwer, E. B. Brouwer, G. MacLaurin, M. Lee, D. Parks and J. A. Ripmeester, Supramolecular Chem., 8, 361 (1997)
40. T. Akiya, T. Shimazaki, M. Oowa, M. Matsuo, and Y. Yoshida, Internat. J. Thermophys., 20, 1753 (1999)
41. D. Liang, K. Guo, R. Wang and S. Fan, Fluid Phase Equil., 187-188, 61 (2001)
42. S. Imai, K. Okutani, R. Ohmura and Y. H. Mori, J. Chem. Eng. Data, 50, 1783 (2005).
43. J. C. Seitz, J. D. Pasteris and B. Wopenka, Geochim. Cosmochim. Acta, 51, 1651 (1987).
44. A. K. Sum, R. C. Burruss and E. D. Sloan, J. Phys. Chem. B, 101, 7371 (1997).
45. T. Uchida, T. Hirano, T. Ebinuma, H. Narita, K. Gohara, S. Mae and R. Matsumoto, A.I.Ch.E. J., 45, 2641 (1999).
46. N. J. English and J. M. D. MacElroy, J. Comput. Chem., 24, 1569 (2003).
47. N. J. English, J. K. Johnson and C. E. Taylor, J. Chem. Phys., 123, 244503 (2005).
48. A. A. Chialvo, M. Houssa and P. T. Cummings, J. Phys. Chem. B, 106, 442 (2002).
49. J. A. Greathouse, R. T. Cygan and B. A. Simmons, J. Phys. Chem. *B*, 110, 6428 (2006).
50. Z. T. Cao, J. W. Tester, K. A. Sparks and B. L. Trout, J. Phys. Chem. B, 105, 10950 (2001).
51. B. J. Anderson, J. W. Tester and B. L. Trout, J. Phys. Chem. B, 108, 18705 (2004).
52. J. Vatamanu and P. G. Kusalik, J. Phys. Chem. *B*, 110, 15896 (2006).
53. O. K. Forrisddahl, B. Kvamme and A. D. Haymet, J. Mol. Phys., 89, 819 (1996).
54. J. B. Klauda and S. I. Sandler, Chem. Eng. Sci., 58, 27 (2003).
55. P. M. Rodger, Annals of the New York Academy of Science, 912, 474 (2000).
56. C. Moon, P. C. Taylor and P. M. Rodger, J. Am. Chem. Soc., 125, 4706 (2003).
57. M. T. Storr, P. C. Taylor, J. P. Monfort and P. M. Rodger, J. Am. Chem. Soc., 126, 1569 (2004).
58. H. Nada, J. Phys. Chem. B, 110, 16526 (2006).
59. S. Alavi, J. A. Ripmeester and D. D. Klug, J. Chem. Phys., 123, 024507 (2005).

60. S. Alavi, J. A. Ripmeester and D. D. Klug, J. Chem. Phys., 124, 014704 (2006).
61. J. B. Klauda and S. I. Sandler, J. Phys. Chem. B, 106, 5722 (2002).
62. M. H. F. B. Sluiter, V. Rodion, A. Jain, and V. R. Belosludov, H. Adachi, Y. Kawazoe, K. Higuchi and T. Otani, Lec. Notes Comput. Sc., 2858, 330 (2003).
63. P. Dauber-Osguthorpe, V. A. Roberts, D. J. Osguthorpe, J. Wolff, M. Genest and A. T. Hagler, Proteins: Struct., Funct., Genet., 4, 31 (1998).
64. R. W. Bradshaw, B. A. Simmons, E. W. Majzoub, W. M. Clift and D. E. Dedrick, "Clathrate Hydrates for Production of Potable Water", Materials Science of Water Purification, Materials Research Society, 2006, San Francisco.
65. R. Ohmura, M. Ogawa, K. Yasuoka and Y. H. Mori, J. Phys. Chem. B, 107, 5289 (2003).
66. I. Kobayashi, Y. Ito and Y. Mori, Chem. Eng. Sci., 56, 4331 (2001).
67. M. Komiyama and M. Kobayashi, J. Phys. Chem. B, 103, 10651 (1999).
68. B. J. Delley, Chem. Phys., 92, 508 (1990).
69. B. J. Delley, Chem. Phys., 113, 7756 (2000).
70. R. K. McMullan and A. Kvick, Acta Crystallogr. B, 46, 390 (1990).
71. J. P. Perdew and Y. Wang, Phys. Rev. B, 45, 13244 (1992).
72. E. B. Wilson, P. C. Cross and J. C. Decius, *Molecular Vibrations: The Theory of Infrared and Raman Vibrational Spectra*; Courier Dover: New York, 1980.
73. O. Teleman, B. Jonsson and S. Engstrom, Mol. Phys., 60, 193 (1987).
74. D. Frenkel and B. Smit, *Understanding Molecular Simulation: From Algorithms to Applications*, 2nd ed., Academic Press: San Diego, 2002.
75. J. W. Glen, Phys. Kondens. Materie, 7, 43 (1968).
76. C. McBride, C. Vega, E. Sanz, L. G. MacDowell and J. L. F. Abascal, Mol. Phys., 103, 1 (2005).
77. C. Vega, E. Sanz, E. and J. L. F. Abascal, J. Chem. Phys., 122, 114507 (2005).
78. D. C. Young, *Computational Chemistry: A Practical Guide for Applying Techniques to Real World Problems*, John Wiley and Sons, Inc., New York, 2001.
79. A. Ruzsinszky, J. P. Perdew and G. I. Csonka, J. Phys. Chem. A, 109, 11006 (2005).
80. C. Tuma and J. Sauer, J. *Phys.* Chem. Chem. Phys., 8, 3955 (2006).
81. R. F. Hout and W. J. Hehre, J. Am. Chem. Soc., 105, 3728 (1983).
82. D. W. Davidson, Clathrate Hydrates, In *Water: A Comprehensive Treatise, Volume 2*; Franks, F., Ed.; Plenum Press: New York, 1973; pp 130.
83. G. A. Jeffrey and W. Saenger, *Hydrogen Bonding in Biological Structures*, Springer-Verlag: New York, 1991.
84. K. Nakanishi and P. H. Solomon, *Infrared Absorption Spectroscopy*; Holden-Day: New York, 1977.
85. J. R. Scherer and R. G. Snyder, *J. Chem. Phys.*, 67, 4794 (1977).
86. M. Yousuf, S. B. Qadri, D. L. Knies, K. S. Grabowski, R. B. Coffin, J. W. Pohlman, Appl. Physics A, 78, 925 (2004).
87. T. Akiya, T. Shimazaki, M. Oowa, M. Matsuo, and Y. Yoshida, Internat. J. Thermophys., 20, 1753 (1999)
88. R. W. Bradshaw, "Clathrate Hydrate Formation by Gaseous Guest Species in Saline Water", Sandia National Laboratories, report in preparation (2008)
89. M. S. Rahman, M. Ahmed and X. D. Chen, Separation Purification Reviews, 35, 59 (2006).

90. S. M. Shaik, T. H. Ooi and P. O. Simo, "The Prospect of Using LNG Regasification as a Heat Sink for Seawater Desalination", A. I. Ch. E. Annual Meeting, San Francisco, CA, Nov. 16, 2006.
91. M. Landau and A. Martindale, Desalination, 3, 318 (1967)
92. J. R. Rains, Mouchel-Parkman, Ltd., Surrey, UK, Telephone communication to R. W. Bradshaw, April 7, 2007.

Distribution

1 Prof. E. H. Majzoub
University of Missouri
Dept. of Physics and Astronomy
503J Benton Hall
One University Blvd.
St. Louis, MO 63121

1	MS 0123	D. L. Chavez, 1011 (LDRD Office)
1	MS 0754	M. J. Rigali, 6316
1	MS 0754	R. T. Cygan, 6316
3	MS 0754	J. A. Greathouse, 6316
1	MS 0754	T. M. Mayer, 6316
1	MS 9161	B. A. Simmons, 8755
1	MS 9403	T. J. Shepodd, 8778
1	MS 9409	D. E. Dedrick, 8757
3	MS 9403	R. W. Bradshaw, 8778

1	MS 0899	Technical Library, 9616
3	MS 9018	Central Technical Files, 8945-1
1	MS 9021	Classification Office, 8511 For DOE/OSTI
1	MS 0161	Patent and Licensing Office, 11500


Sandia National Laboratories